Marcel Rossetti da Silva

SINTERING SIMULATION OF NICKEL AND ALUMINA COMPOSITE USING DISCRETE ELEMENT METHOD

Master´s Dissertation presented to the Graduate Program in Chemical Engineering of the Federal University of Santa Catarina, as a requirement for obtaining the Master degree in Chemical Engineering.

Supervisor at UFSC:
Prof. Dr. Dachamir Hotza
Supervisor at TUHH, Germany:
Prof. Dr. Robert Besler

Florianópolis
2016

Ficha de identificação da obra elaborada pelo autor,
através do Programa de Geração Automática da Biblioteca Universitária da UFSC.

Silva, Marcel Rossetti da
Sintering simulation of nickel and alumina composite using Discrete Element Method / Marcel Rossetti da Silva ; orientador, Dachamir Hotza ; coorientador, Robert Besler. Florianópolis, SC, 2016.
106 p.

Dissertação (mestrado) - Universidade Federal de Santa Catarina, Centro Tecnológico. Programa de Pós-Graduação em Engenharia Química.

Inclui referências

1. Engenharia Química. 2. Discrete Element Method. 3. Sintering . 4. Simulation. 5. Composite Material. I. Hotza, Dachamir. II. Besler, Robert. III. Universidade Federal de Santa Catarina. Programa de Pós-Graduação em Engenharia Química. IV. Título.

Sintering Simulation of Nickel and Alumina Composite Using Discrete Element Method

por

Marcel Rossetti da Silva

Dissertação julgada para obtenção do título de **Mestre em Engenharia Química**, área de Concentração de **Desenvolvimento de Processos Químicos e Biotecnológicos** e aprovada em sua forma final pelo Programa de Pós-Graduação em Engenharia Química da Universidade Federal de Santa Catarina.

_____
Prof. Dr. Dachamir Hotza
orientador

_____
Prof. Dr. Robert Besler
coorientador

_____
Prof.ª Dr.ª Cintia Soares
coordenadora

Banca examinadora:

_____
Prof.ª Dr.ª Cintia Soares

_____
Prof. Dr. Aloisio Nelmo Klein

_____
Prof. Dr. Rolf Janßen
(videoconferência)

Florianópolis, 2 de dezembro de 2016.

To my family and friends who have always supported my dreams!

ACKNOWLEDGEMENTS

Firstly, I would like to thank my father and mother, who have always believed in my capabilities and are very proud of my achievements. Thanks to my three brothers, they are a fundamental piece for the person I became today. Special thanks to my brother Demian that has made my academic life to be possible. In addition, I need to thank my friends *Moreiras*, from whom I have learned so much in my years at university. Their support and friendship have been essential to reach where I am. Special thanks to my wonderful girlfriend Nati that has always pushed me forward to finish this journey. Her affection and help have been very important in my life.

Moreover, I would like to thank professor Dachamir Hotza. He has always been kind, helpful and believed in my capacities. I consider myself a lucky guy to meet him and this work would not be possible without his help. He is a great inspiration for my personal and professional academic life. I have also to thank the opportunity to go to Germany.

Special thanks to my supervisors at TUHH – Germany, Dr. Robert Besler and Prof. Rolf Janssen, who have received me in Hamburg very well. I am very grateful by the opportunity, the experience and knowledge shared with me. I could learn so much during that year. The work there has brought me so many good things that could not imagine at the beginning. Thanks also for all people from the group of the Institute of Advanced Ceramics. Thanks to Prof. Maksym Dosta for his help and support. Thanks to Prof. Hazim Ali Al-Qureshi for the help and advices, who is also responsible for my time in Germany.

This work has been also possible thanks to the financial support from the Brazilian funding agencies CAPES and CNPq.

I also acknowledge all Professors that have taught me during my master degree and undergraduation.

“Once we accept our limits, we go beyond them.”

(Albert Einstein)

RESUMO

Sendo o resultado da combinação de dois ou mais materiais, os materiais compósitos possuem características únicas e são usados em sistemas de engenharia que necessitam alto desempenho e propriedades altamente específicas, como, por exemplo em aeronaves e equipamentos esportivos. Materiais compósitos podem ser produzidos pela "tecnologia do pó", na qual basicamente o pó metálico e/ou cerâmico é compactado e, por fim, sinterizado. A sinterização é um processo de densificação, onde ocorre a consolidação do material e é a etapa responsável por conferir força e resistência à peça. Assim, nota-se que o controle dessa etapa é determinante para se atingir as propriedades desejadas à peça final. Em paralelo, simulações numéricas do processo de sinterização são uma alternativa em relação a custosos e longos experimentos físicos. Uma metodologia de simulação numérica muito promissora é chamada de Método dos Elementos Discretos (DEM – *Discrete Element Method*). Diferentemente dos métodos contínuos de simulação, o DEM considera cada partícula do sistema como um elemento distinto e é ideal para a simulação de meios granulares, como é o caso da sinterização. Assim, esse projeto tem por objetivo simular e analisar o processo de sinterização em estado sólido de materiais compósitos utilizando o Método dos Elementos Discretos. O software utilizado foi o MUSEN, desenvolvido na Universidade Tecnológica de Hamburgo (TUHH - Alemanha). Os materiais do compósito utilizado nas simulação são níquel (metal) e alumina (cerâmico). Especificamente, esse trabalho visa investigar a influência de diferentes proporções de metal/cerâmico em amostras monomodais (apenas um tamanho de partícula) durante a sinterização. Além disso, a influência de partículas maiores de metal em amostras bimodais também foi analisada. Entre as análises conduzidas, foi avaliado o crescimento do raio de contato das partículas entre os diferentes tipos de contatos: metal-metal, cerâmico-cerâmico e metal-cerâmico. O número de coordenação das partículas com esses 3 tipos de contato também foi investigado. Finalmente, a influência de diferentes parâmetros no comportamento de densificação foi analisada e correlacionada com o crescimento de raio de contato e número de coordenação entre as partículas. A partir dos resultados, foi possível confirmar que a modelagem modificada foi capaz de simular a sinterização de compósitos, mesmo para estruturas interpenetrantes. Os resultados das amostras monomodais foram divididos em três diferentes comportamentos de sinterização: controladas pelo metal, controladas

pelo cerâmico e estruturas interpenetrantes. As amostras controladas pelo metal apresentaram as maiores taxas de densificação e atingiram as maiores densidades relativas ao final da simulação. As partículas de metal (neste caso níquel) possuem um potencial maior para sinterizar mais rápido que a alumina devido ao seus parâmetros cinéticos e energia superficial. Também foi observado que a adição de uma segunda fase com uma menor atividade de sinterização (alumina) reduz a densificação global em comparação com o puro metal e leva mais tempo para atingir a mesma densidade relativa. As estruturas interpenetrantes apresentaram as menores densificações globais dentre todas amostras devido à densificação independente da fase metálica e cerâmica. Esse comportamento conduziu à formação de muitas fissuras e rachaduras ao longo da amostra e a estrutura inicial foi perdida, formando na verdade uma estrutura porosa. Os resultados das amostras bimodais mostraram um crescimento mais lento do raio de contato para partículas maiores de níquel, como é esperado. Entretanto, a densificação global foi maior para amostras com maiores partículas de níquel. Esse comportamento não era esperado, porém pode ser explicado pela configuração das partículas em estruturas interpenetrantes. Nessas estruturas, não existe uma fase "matriz", a fase metálica e cerâmica formam redes contínuas de partículas, chamados de *caminhos de percolação*. Quando partículas menores estão presentes nessas estruturas, elas apresentam maior força de sinterização, rapidamente se atraem, formam longos aglomerados de partículas e a densificação global praticamente não ocorre. Por outro lado, partículas maiores induzem menores forças de sinterização. Assim, as forças viscosas entre contatos alumina-níquel são suficientes para manter esses contatos unidos e, consequentemente, a densificação global pode ser observada.

Palavras-chave: Método dos elementos discretos, sinterização, simulação, compósitos, metal-cerâmico, níquel, alumina.

ABSTRACT

Composite is a class of material made by the combination of two or more materials, which produces a third one with unique characteristics. For this reason, composites have a wide range of engineering applications, such as spacecrafts and sports' equipment. Composite materials can be suitably produced by *Powder Metallurgy*. In this manufacturing process, the blend of different powders is shaped and later sintered at high temperatures for consolidation of the part. Thereby, sintering is considered a densification process, which is responsible for providing strength and stiffness to the material or composite. Moreover, its control is essential to reach the desired properties of the final part. In addition, numerical simulations of the sintering process represent an alternative procedure in relation to the lengthy and costly physical experiments. A well-known simulation technique is the Discrete Element Method (DEM). In contrast to continuum methods, DEM considers every particle of the system as a single element and it is recommended to simulate granular media, such as sintering. Thus, the general purpose of this project is to simulate and analyze the solid-state sintering process of composite materials when both materials are sintering using DEM. The software used is the MUSEN system, developed at TUHH – Germany. The materials chosen for the composite are nickel (metal) and alumina (ceramic). Specifically, the present work aims to investigate the influence of varying contents of metal/ceramic in monosized samples during sintering. These contents range from metal volume fraction of 0.9 to 0.1, and include pure metal and ceramic bodies. Furthermore, the effect of larger metallic particles in the sample is also investigated for a constant metal volume fraction of 0.6. Among the analyses carried out, the contact size growth was evaluated considering the interfaces metal-metal, ceramic-ceramic and metal-ceramic. The coordination number of the particles within these three contacts is also analyzed. Finally, the influence of the varied parameters on the densification behavior is investigated and correlated with the contact size growth and coordination number evolution. The results have shown that the special modeling was capable to simulate sintering of composites even in case of interpenetrating structures. The simulation results of the monosized packing can be divided in three different sintering behaviors: metal-controlled, ceramic-controlled and interpenetrating structures. The metal-controlled samples have shown the highest densification rates and relative density evolution, as one

might expect. The nickel particles have higher potential to sinter faster than alumina due to their kinetic parameters and surface energy. Hence, metal particles induce high forces to shrink the system and indirectly transfer forces to the sintering of ceramic phase. Interpenetrating structures have shown the lowest overall densification due to independent densification of metal and ceramic phase. It has led to large cracks through the samples and the initial structure has been lost. The results of bimodal packings have shown a slower growing of the contact radius for larger nickel particles, as expected. However, the global densification has been higher for samples with larger nickel particles. This unexpected behavior can be explained due to the particle configuration and distribution of forces in the interpenetrating structures. Smaller particles induce higher forces, quickly agglomerate themselves and are not capable to drive a global densification. On the other hand, larger particles induce weaker sintering forces. Thereby, the resistance force between nickel-alumina contacts is high enough to keep these contacts attached and, consequently, a global densification can be observed.

Keywords: Discrete Element Method (DEM), sintering, simulation, composites, metal/ceramic, nickel, alumina.

LIST OF FIGURES

LIST OF TABLES

LIST OF SYMBOLS

Latin letters

a_s	Contact radius	m
a_s^*	Average contact radius	m
A	Total surface area of the compact	m²
D_b	Diffusion coefficient	m²/s
D_{0b}	Diffusion coefficient pre-exponential factor	m²/s
$\vec{F}_n$	Force acting on normal direction	N
$\vec{F}_t$	Force acting on tangential direction	N
h	Overlap between two particles	m
$\vec{i}_n$	Unit vector in the normal direction	-
I	Moment of inertia	kg·m²
k	Boltzmann constant	m²·kg/(s²·K)
m	Mass	kg
Q_b	Activation energy	kJ/mol
$\vec{r}$	Vector position	m
R	Particle radius	m
$\mathbf{R}^*$	Equivalent radius	m
R_g	Ideal gas constant	J/(K·mol)
t_s	Simulation time	s
t_{save}	Saving time step	s
Δt	Time step	s
T	Temperature	K or °C
$\vec{T}$	Torque	N·m
T_m	Melting point	°C
$\vec{u}$	Vector velocity	m/s

Greek letters

$\boldsymbol{\alpha}$	Parameter related to the dominant diffusion mechanism	-
$\boldsymbol{\beta}$	Parameter related to the dominant diffusion mechanism	-
$\Delta_{\boldsymbol{b}}$	Diffusion parameter	$m^4 \cdot s/kg$
$\boldsymbol{\gamma_s}$	Specific surface energy	J/m^2
$\boldsymbol{\delta_b}$	Grain-boundary thickness	m
$\boldsymbol{\eta_{par}}$	Sliding friction coefficient	-
$\boldsymbol{\rho_m}$	Material density	kg/m^3
$\boldsymbol{\sigma}$	Sintering stress	N/m^2
$\boldsymbol{\varphi}$	Ratio between surface and grain boundary diffusion	-
$\boldsymbol{\Omega}$	Mean atomic volume	m^3
$\vec{\boldsymbol{\omega}}$	Angular velocity	rad/s

LIST OF ABBREVIATIONS

ACN	Average Coordination Number
ACR	Average Contact Radius
Al_2O_3-Al_2O_3	Alumina-Alumina contacts
CN	Coordination Number
DEM	Discrete Element Method
DR	Densification Rate
Ni-Al_2O_3	Nickel-Alumina contacts
Ni-Ni	Nickel-Nickel contacts
RD	Relative Density

TABLE OF CONTENTS

1 INTRODUCTION

The current need for highly efficient materials with very specific properties to be used in engineering systems has stimulated the development of new composites. This class of materials is made by the combination of two or more materials, which produces a third one with unique characteristics if compared to the materials separately. For this reason, composites have a wide range of engineering applications, such as spacecrafts, airplanes, automobiles, boats, sports' equipment, bridges, buildings and others [1].

Composite materials, mainly particulate composites, can be suitably produced by *Powder Metallurgy*. In this manufacturing process, the blend of different powders is shaped and later sintered at high temperatures for consolidation of the part. During sintering, the particles of the powder create solid bonds between each other in order to reduce the total surface energy of the system so that the porosity of the body is decreased during the process. Hence, sintering is considered a densification process, which is responsible for providing strength and stiffness to the material or composite. Moreover, its control is essential to reach the desired properties of the final part [2].

In addition, numerical simulations of the sintering process represent an alternative procedure in relation to the lengthy and costly physical experiments, so that time and costs may be reduced. Moreover, if the simulations are well dimensioned, not only the scientific aspects of the physical phenomena are addressed, but also industrial aspects may be incorporated into the models in order to make process more efficient in terms of energy and costs. Thus, the main goal of simulation developments in powder metallurgy is to describe analytically the complete process chain from the powder filling into the die to the final in-service behavior, in order to optimize material and process properties further [3].

A well-known simulation technique is the Discrete Element Method (DEM). In contrast to continuum methods, DEM considers every particle of the system as a single element, which interacts by modeling of forces. Continuum methods are based on phenomenological models that rely on empirical assumptions about the macroscopic behavior of materials. Thereby, they neglect effects due to the microstructure of materials such as heterogeneities and anisotropy. In DEM, these microstructural effects are naturally taken into account. Particularly for sintering simulation, DEM can also be used to

investigate the contact size between particles, coordination number (number of contacting particles), particles rearrangement, particles size distribution, cracks formation, among others. Furthermore, macroscopic behavior such as densification can be analyzed conveniently.

DEM has been used to simulate solid-state sintering in three dimensionally system in the last ten years, including the works of Martin et al. (2006) [4] and Henrich et al. (2007) [3]. Considering DEM simulation of powder mixtures, only few references can be found in the literature [5,6]. In such works, the authors have considered the ceramic phase as hard inclusions, which do not sintering. Therefore, no work was reported so far, in which both metallic and ceramic materials are sintering.

In this context, the general purpose of this master thesis is to simulate free solid-state sintering process of composite materials when both materials are sintering using Discrete Element Method (DEM). The material parameters used in the simulations are related to nickel (metal) and aluminum oxide (alumina; ceramic). As free solid-state is the sintering technique simulated, neither liquid phase nor pressure is considered. The sintering temperature used through the simulations is below the melting point of both materials, but high enough for both ceramic and metal sinter.

Specifically, the present work aims to investigate the influence of varying contents of metal/ceramic in monosized samples during sintering. These contents range from metal volume fraction of 0.9 to 0.1, and include pure metal and ceramic bodies. In order to investigate whether the lack of periodic boundary conditions affect the simulation results, a simulation of samples with higher number of particles is also performed.

Furthermore, the effect of larger metallic particles in the sample is also investigated for a constant metal volume fraction of 0.6. Among the analyses carried out, the contact size growth was evaluated considering the interfaces metal-metal, ceramic-ceramic and metal-ceramic. The coordination number of the particles within these three contacts is also analyzed. Finally, the influence of the varied parameters on the densification behavior is investigated and correlated with the contact size growth and coordination number evolution.

2 THEORETICAL BACKGROUND

This chapter is divided into four topics. First of all, composite materials are described and their classification is presented. Secondly, the theory of sintering and the main features of powder metallurgy are described. The phenomena that take place during sintering as well as the parameters which influence the sintering behavior are discussed. In third place, the discrete element method is introduced and some important works in the literature are presented. Finally, the mathematical model that described the sintering phenomenon is presented.

2.1 COMPOSITE MATERIALS

Composites are a class of materials formed by the combination of two or more different materials that are mechanically or metallurgically bonded together. The material components in composites can be metals (titanium, nickel, etc.), ceramics (aluminum oxide, tungsten carbide, etc.) and organics (epoxy, PMMA, etc.). The key advantage of composites is that they usually exhibit the best qualities of their components or constituents and often some properties that neither component possesses. Such properties depend on the application that the composite is designed for and they may be a combination of stiffness, weight, strength, high-temperature performance, corrosion resistance, hardness, conductivity, among others. Hence, composite materials can reach a performance required by both engineering advanced systems and domestic applications where very specific properties are needed [1].

The origin of the distinct discipline of composite materials is reported since the beginning of the 1960s. However, the use of composite materials is much older. For example, medieval swords and armor were constructed with layers of different metals. In the latest 50 years, the demand for materials with specific properties and high-performance system has increased substantially in several fields as aerospace, energy and civil construction. Airplanes represent a typical application, where one material must exhibit light weight, high strength, stiffness and fatigue resistance [1].

A common classification of composite materials is related to their structural constituents as:

- laminar or layered composites;
- fiber-reinforced composites;
- particulate composites.

Laminar composites consist of layers of at least two different materials that are bonded together. They are used to provide properties such as reduced cost, enhanced corrosion resistance or wear resistance, electrical insulation or conductivity, unique expansion characteristics, lighter weight, improved strength or altered appearance. Safety glass is an example of this category in which a layer of polymeric adhesive is placed between two pieces of glass and serves to retain the fragments when the glass is broken [7].

Fiber-reinforced composites comprise continuous or discontinuous thin fibers that are embedded in a matrix of another material. The matrix supports and transmits forces to the fibers, protects them from the environment and provides ductility and toughness, while the fibers carry most of the load and impart enhanced stiffness. Glass-fiber-reinforced resins represent an important example of fibrous composites. With them it is possible to produce lightweight materials with high strength and high stiffness. In such a case, glass fibers about 10 μm in diameter are bonded in a variety of polymers, generally epoxy or polyester resins. Current uses of glass-fiber-reinforced plastics include sporting goods (snowboards), boat hulls and bathtubs [7].

Particulate composites are made of discrete particles of one material surrounded by a matrix of another material. The particles can be either metallic or nonmetallic, as well as the matrix. Concrete is a classic example, consisting of sand and gravel particles surrounded by hydrated cement, where the particles are rather coarse. Another example are gridding and cutting wheels, which are often formed by bonding abrasives, such as aluminum oxide, silicon carbide, cubic boron carbide, or diamond, in a matrix of glass or polymeric material. The purpose of particulate composites can be also to increase the toughness, by addition of cemented carbide in a metal matrix of cobalt. Combining tungsten powder and powdered silver or copper produces high conductivity and resistance to wear [7].

Even though the most common kind of particulate composites consist of particle-matrix composites, there is another sort of structure for particulate composites. When the volume fraction of the particulate

phase exceeds a certain amount, the particles start to form a continuous network of particles. This kind of structure is called *percolation network*. The volume fraction limit depends on the particle size distribution width. For a wide particle size distribution, the limit value is about 10% of the volume fraction, whereas for monosized particles its value is about 30% [5]. In such a case, the particle and matrix phase cannot be distinguished from each other, and this definition is not valid anymore. Therefore, this sort of system is called *interpenetrating structures*, where both phases form continuous network in different directions through the sample and distinct properties may be developed due to this new sort of structure.

Composite materials, particularly particulate composites, may be conveniently produced by powder metallurgical techniques. In this case, the main advantage is that metal and ceramic powder can be mixed homogeneously and in varying amounts in order to obtain different structures and properties. Moreover, the technique versatility allows producing parts with a wide variety of shapes and sizes [7].

2.2 POWDER METALLURGY

Powder metallurgy is a process in which fine powdered materials are blended and pressed into a desired shape (compacted). The compacted part is called *green body*. Then, the green body is heated (sintered) to establish desired properties. This process has expanded rapidly due to the recognition of the distinct advantages in terms of materials utilization, ease of components manufacturing, cost/energy saving and other factors. Through the manufacturing process, sintering is an essential step, where the compacted material is heated in a controlled atmosphere and temperature to obtain the required density and strength [7]. Figure 2.1 shows a general processing pattern to produce sintered parts [8]. Every step through the process has great influence on the sintering behavior and consequently in the shape and properties of the end product.

The technique used to produce the powder (chemical reduction, electrolytic deposition, precipitation from solution, etc.) has influence on the size, size distribution, shape and agglomeration of the particles. For instance, smaller particles present higher surface energy and would increase the sintering rate [9].

Figure 2.1: General fabrication pattern of sintered parts [8].

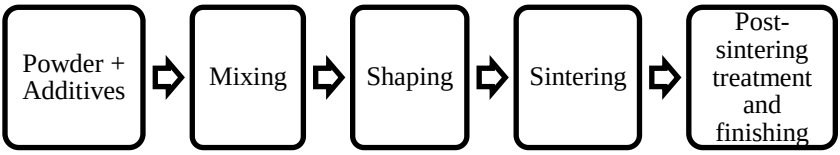

Additives used during powder preparation can change the shaping and/or sintering behavior, such as lubricants that reduce the friction between particles and improve their rearrangement during compaction [9].

Die compaction, isostatic pressing and slip casting represent some possible techniques to be used in the shaping or forming step. Depending on the compaction technique employed, varying initial densities (so-called *green density*; initial density of the sample that will be sintered) may be obtained. The green density of a compact has direct influence on the densification behavior and hence on the strength of the product [9].

Although such steps before sintering are very important for the overall process, they are out of scope of this work and are not discussed in details. For instance, Richerson's book [9] explores the topic deeply.

2.3 FUNDAMENTALS OF SINTERING

Sintering is a processing technique used to manufacture density-controlled materials and components from metal or/and ceramic powders by applying thermal energy. Sintering belongs to powder manufacturing technology and represents a crucial step for reaching the desired mechanical and other properties. Their application fields range from firing ceramic pots to fabrication of complex, high-performance shapes, such as medical implants and gas turbines [10].

In fact, sintering is one of the oldest human technologies, originating in the prehistoric era with firing of pottery to add strength. Ancient Incas used this technique to produce jewelry and other artifacts from precious metal powder. Many other sintered ceramic structures can be found around the world in ancient civilizations (Egypt, Mesopotamia, etc), such as bricks, porcelains, vessels, etc. [11].

The process has been used through the centuries for several purposes, but scientific understanding and controlled experiments have only been developed in the 20th century. One of the earliest controlled

experiments was conducted by Muller in 1935. He sintered compacts of NaCl powder for a variety of times at several temperatures and evaluated the degree of sintering by measuring the strength of fracture [9].

Ever since, remarkable developments have been done. The application of scanning electron microscopy, transmission electron microscopy, and lattice imaging has allowed the investigation of microstructure changes at different stages of sintered parts, as well as the density and shrinkage evolution may be plotted as function of time [9]. Figure 2.2 shows the empirical curve of the bulk density of fused silica prepared by solid-state sintering method as function of sintering time [12].

Figure 2.2: Density of fused silica prepared by solid-state sintering method as function of sintering time [12].

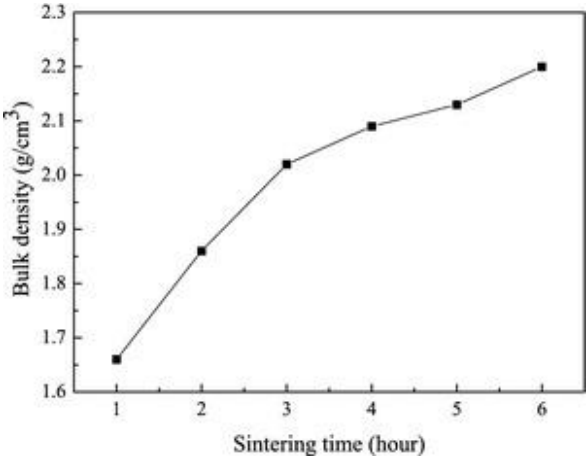

2.3.1 Sintering Process Overview

According to German [2], "*Sintering is a thermal treatment for bonding particles into a coherent, predominantly solid structure via mass transport events that often occur on the atomic scale. The bonding leads to improve strength and lower system energy*."

During sintering, a consolidation of loose or weakly bonded powder (*green body)* occurs by heating the material in a sintering furnace at temperatures below its melting point but high enough to permit solid-state diffusion. Typical sintering temperatures, for example,

can range between 750-1000 °C for copper and 1350-1450 °C for cemented carbides [7].

The main driving force for sintering is the reduction of the free surface energy of powdered compacts, due to the elimination of internal surface area associated with the pores. In the beginning of the process, contacting particles start to create connections (necks). As sintering proceeds, the high temperatures allow atoms to move and the neck grows, forming solid bonds between particles. Figure 2.3 shows a scanning electron micrograph of bronze particles after sintering at 800 °C, where necks between particles can be observed clearly [10].

Figure 2.3: Scanning electron micrograph of the sintering necks formed between bronze particles after sintering at 800 °C [10].

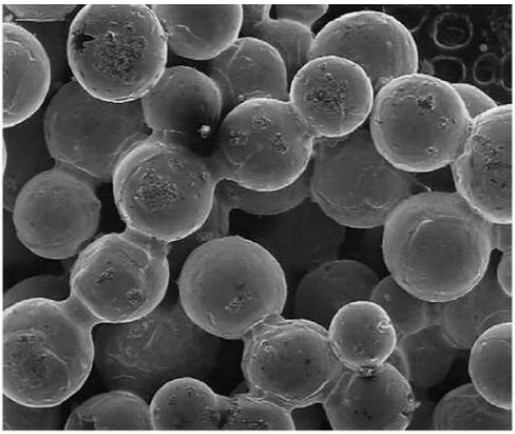

Throughout sintering process, the pores reduce in size, whereas the density increases and product dimensions change (shrinkage). As a result, the sintered part may have its strength, stiffness, ductility, toughness, and electrical and thermal conductivities increased if compared to the green body [7].

There are different sintering techniques and the phenomena that take place during the process change depending on the technique applied. Figure 2.4 shows a general categorization of sintering techniques.

As the first differentiation, sintering can be carried out with or without an external pressure (pressure-assisted and pressureless, respectively). Most industrial sintering is performed without an external pressure. Pressureless sintering is divided into liquid phase sintering or

solid-state sintering. Liquid phase sintering occurs when at least one material melts during the process and a liquid is present in the system. Solid-state sintering occurs when the powder compact is densified wholly in a solid state at the sintering temperature. In solid-state, single phase is considered when only one material is sintered. Mixed phase occurs when a mixture of at least two kinds of powders is sintered to form composites and alloys [2].

Figure 2.4: The taxonomy of the sintering technique [2].

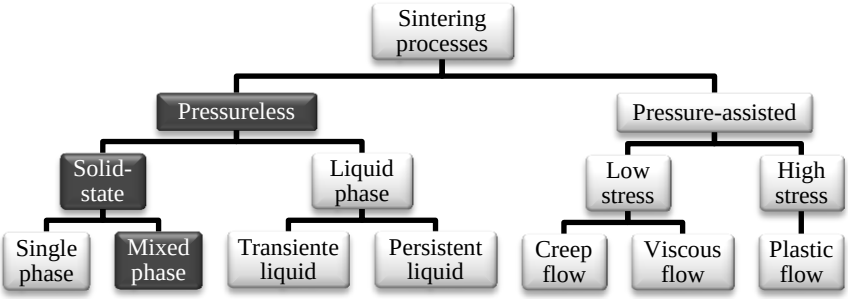

The scope of the present work is the mixed phase in solid-state sintering (black part in Figure 2.4). Therefore, the following sections introduce the concepts and phenomena related to this technique. Liquid phase and pressure-assisted sintering are not considered nor their related phenomena.

A wide variety of parameters affects sintering and they may be divided into two categories: material and process variables. Table 2.1 shows the main variables that influence the behavior during sintering [8].

Table 2.1: Variables that affect the sintering behavior [8].

Process variables	**Material variables**	
	Powder	**Chemistry**
Temperature	shape	composition
Time	size	impurity
Pressure	size distribution	non-stoichiometry
Atmosphere	agglomeration	homogeneity
Heating and cooling rate	mixedness	

The process parameters are mostly thermodynamic variables and have great (and complex) influence in the sintering kinetics and the final properties of the sintered part. For example, higher temperatures induce higher sintering rates and can improve the final properties though increase the expense and complicate the process control.

The variables related to the material are also of fundamental importance to the process. For example, smaller particles have higher total surface energy and then higher driven force for sintering. Either it means that faster sintering (lower sintering time) or lower sintering temperatures can be applied. For compacts containing more than two kinds of powder, the homogeneity is of prime importance to result in a sintered part with homogeneous and isotropic properties [8].

2.3.2 Thermodynamics of Sintering

From the thermodynamic point of view, sintering is an irreversible process in which surface energy of the particles plays the fundamental role. Surface energy induces some phenomena and it is important to distinguish them [8].

In order to reduce the total surface energy of the system, the main phenomena that take place during sintering are densification and grain growth. The total surface energy of a powder compact is expressed as $\boldsymbol{\gamma_s A}$, where $\boldsymbol{\gamma_s}$ is the specific surface energy and $\boldsymbol{A}$ the total surface area of the compact. The reduction of the total surface energy of the system can be expressed as [8]:

$$\Delta(\boldsymbol{\gamma_s A}) = \Delta\boldsymbol{\gamma_s A} + \boldsymbol{\gamma_s}\Delta\boldsymbol{A} \tag{2.1}$$

Then, the change in surface energy $\Delta\boldsymbol{\gamma_s}$ is due to densification, whereas the change in the surface area $\Delta\boldsymbol{A}$ is due to grain growth.

On the other hand, for the neck formation and growth (and consequently densification and grain growth) a mechanism for matter transport must be present. The specific energy and curvature of the particle surface provide an effective stress on the atoms under the surface. For a curved surface with principal radii of curvature $\boldsymbol{R_a}$ and $\boldsymbol{R_b}$, this stress $\boldsymbol{\sigma}$ is proportional to the surface energy $\boldsymbol{\gamma_s}$ and is given by Laplace's equation [10]:

$$\boldsymbol{\sigma} = \boldsymbol{\gamma_s}\left(\frac{\mathbf{1}}{\boldsymbol{R_a}} + \frac{\mathbf{1}}{\boldsymbol{R_b}}\right) \tag{2.2}$$

Because the stress in the neck region is different from the neighboring region, atomic motion occurs to remove this gradient. Usually, atomic motions take place often via diffusional solid-state mechanisms. The high temperatures at which sintering are normally led are essential to allow the atoms to move. Such mechanism will be discussed in details further on.

2.3.3 Stages of Solid-State Sintering

Solid-state sintering is often divided into three overlapped stages: initial, intermediate and final stage. They are related to the sequence of physical changes that occur as particles bond together and the porosity disappears. Figure 2.5 shows a representation of those stages as sintering proceeds [10]. Figure 2.6 shows a typical densification curve of sintering versus time [8], which represents the three stages and their relative density.

Figure 2.5: Representation of the sintering stages with a focus on the changes in pore structure during sintering [10].

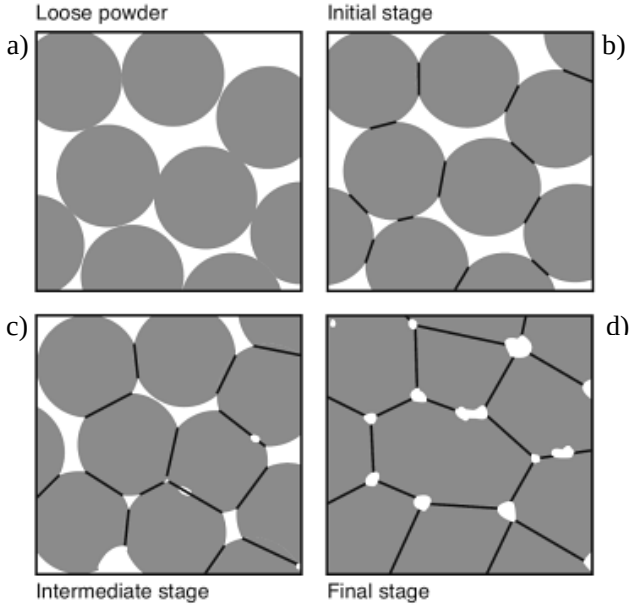

Figure 2.5 a) shows particles as a loose powder with a relative density (green density) defined by the compaction technique used [10]. Figure 2.5 b) represents the initial stage in which is characterized by the rearrangement of particles and the initial neck formation at the point of contact between particles. The rearrangement consists of slight movements of adjacent particles to increase the number of points of contact. This mechanism can partially heal voids and defects present along the sintered part. Normally curvature gradients inherent to the powder dictate the sintering behavior. As it is observed in Figure 2.6, the contribution of this stage on the compact shrinkage is only 2-3% at the most within a negligible time if the total sintering time is considered [8].

In the intermediate stage (Figure 2.5 c), the size of the necks grows and the center of the original particles moves closer together. This results in shrinkage and the porosity decreases, so that the relative density can reach up to ~93%, as shown in Figure 2.6. During the second-stage, the pores are tubular and interconnected (open porosity) [10].

Figure 2.6: Schematic showing a typical densification curve of a powder compact and the three stages of sintering [8].

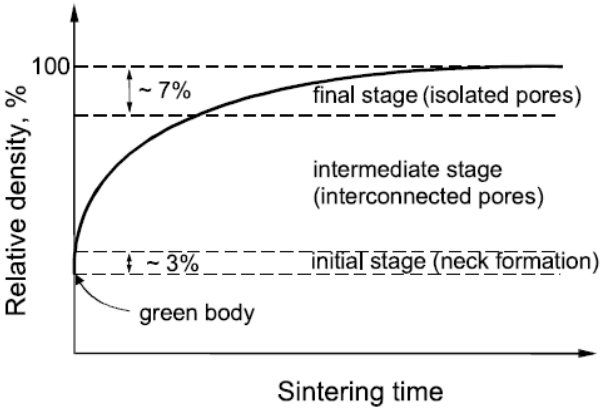

The final stage of sintering (Figure 2.5 d) corresponds to the elimination of the last ~7% of porosity, in which the pores are no longer interconnected and become isolated. At this stage, grain growth plays a fundamental role in pore removal and porosity reduction. As observed in Figure 2.6, this stage is the slowest one and grain growth must be well controlled to achieve maximum removal of porosity. For example, if

grain growth is too rapid, the grain boundaries can move faster than the pores and leave them isolated inside a grain. As the grain continues to grow, the pore becomes further separated from the grain boundary and it has a lower chance to be eliminated [9].

2.3.4 Kinect Mechanisms of Solid-State Sintering

The reduction of the total surface energy of the system as driving force for sintering induces some kinetic mechanisms for matter transport. There are two main mechanisms in sintering: surface transport and bulk transport [10]. Surface transport, such as surface diffusion, vapor transport and lattice diffusion from the particle surface, results in neck growth without promoting shrinkage or densification of the system. In this case, atoms come to the neck from the particle surface. It means the atoms are rearranged along the surface and the interparticle distance is not reduced [8].

On the other hand, in bulk transport mechanism the mass comes from the particle interior to be deposited at the neck, resulting in approximating the particles centers. Hence, this class of mechanism is responsible, beyond the neck growth, for densification and shrinkage of the system. Bulk transport includes grain boundary diffusion, lattice diffusion from grain boundary (also called volume diffusion) and viscous flow [8]. Table 2.2 lists the major mechanisms for matter transport and their related parameters. Figure 2.7 shows a schematic representation for two sintering particles including the matter transport paths listed in Table 2.2.

Table 2.2: Material transport mechanisms during sintering [8, 10].

Material transport mechanism	Material source	Material sink	Densification
1. Surface diffusion	Particle surface	Neck	No
2. Lattice diffusion	Particle surface	Neck	No
3. Vapor transport	Particle surface	Neck	No
4. Grain boundary diffusion	Grain boundary	Neck	Yes
5. Lattice diffusion	Grain boundary	Neck	Yes
6. Viscous flow	Bulk grain	Neck	Yes

Throughout sintering process, the dominant transport mechanism acting on the particles depends on temperature, kind of

material and stage of sintering. Relatively to the melting temperature of the material, bulk transports are dominant at higher temperatures, whereas surface transports are dominant at lower temperatures [10].

Amorphous materials, such as glasses and polymers, sinter in a distinct way if compared to crystalline materials, since amorphous materials lack grain boundaries. These materials sinter by viscous flow (path 6 in Figure 2.7) involving the deformation of particles and the path along which matter flows is not clearly specified. Viscous flow is driven by capillarity. This mechanism is well described by continuum conservation laws for momentum and mass. Particles coalesce at a rate that depends on the particle size and material viscosity. If the temperature increases, the material viscosity decreases and sintering occurs more rapidly. Thus, sintering temperature plays a fundamental role in sintering of these materials [10].

Figure 2.7: Schematic representation of the paths of sintering mechanisms for a system of two particles [8]. Numbers are related to the mechanisms in Table 2.2.

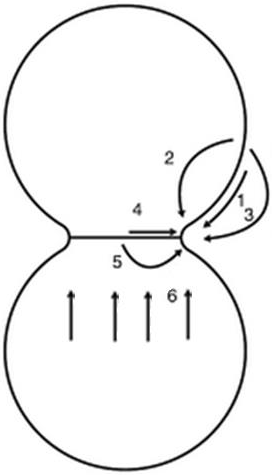

Sintering of polycrystalline materials such as metals and ceramics cannot be described by viscous flow because extremely high stress is needed for matter flows in such structures. The primary mechanism for polycrystalline materials is diffusion, which is related to the movement of atoms under a difference in vacancy concentration in the lattice structure. Usually, more than one kinetic mechanism takes

place simultaneously during this process, as described by the paths 1 to 5 in Figure 2.7.

Vapor transport, represented by path 3 in Figure 2.7, usually occurs in materials with high vapor pressure. A weight loss of the part during sintering can indicate that this mechanism is taking place. However, for most materials the contribution of this mechanism is small and can be neglected [10].

Surface diffusion takes place through the defects on the surface of crystalline materials, as shown by path 1 in Figure 2.7. This mechanism is already active during the heating-up step of sintering because its activation energy is less than other mechanisms. Its contribution to the initiation of sintering is recognized for almost all materials. The influence of surface diffusion decreases as the defects are consumed and the available surface area is lost to the neck growth [10].

Lattice diffusion (volume diffusion) involves the motion of vacancies through the crystalline structure of the solids. Its rate depends on the temperature, particle size and composition. There are two ways for this kind of mechanism, as pointed by the paths 2 and 5 in Figure 2.7. When vacancies flow from the neck to the particle surface (path 2) lattice diffusion does not contribute to densification. Although treated theoretically, there is little evidence for this occurring at significant levels. On the other hand, when vacancies come from the neck to the grain boundary (path 5), the center-to-center approach of two particles is induced and leads to system shrinkage.

Considering that the volume diffusion is active for most materials only at high temperatures (high activation energy), this is not the dominant mass transport during sintering, especially for small powders [10].

Grain boundary diffusion (path 4 in Figure 2.7) is relatively important for sintering of most materials. Indeed, it is the leading mechanism in many cases. The defective character of the grain boundary allows mass flow along the boundary with an activation energy that lays usually between surface and volume diffusion. As surface area is consumed and surface diffusion declines in importance, the simultaneous emergence of new grain boundaries increases the role of grain boundary. On the other hand, grain growth reduces the importance of grain boundary diffusion [10].

Regardless the transport mechanism, once the neck size reaches a thermodynamic equilibrium among surface energy, dihedral angle and

grain boundary energy, further neck growth only occurs due to the grain growth [10].

Therefore, it is clear that mass transport rates, and their influence on neck growth and pores and grain size, are a key factor to understand the sintering process. Models for solid-state sintering usually take into account surface diffusion (prevailing mechanism during initial stage) and grain boundary diffusion (dominant for intermediate stage). Modeling of the final stage of sintering must consider grain growth to be realistic [10].

2.4 DISCRETE ELEMENT METHOD

Several industrial processes as well as many phenomena in nature involve particulate media. The discrete character of the medium results in a complex behavior due to the dynamic interaction between particles and their interaction with surrounding gas or liquid and walls [13]. Traditional theoretical and experimental investigations of the mechanical behavior of granular materials are restricted by the limited quantitative information about what actually happens internally in those systems [14]. Alternatively, numerical simulations using particle length scale is possibly the most powerful tool to understand and reproduce the behavior of such systems.

Cundall and Strack [13] have developed in 1979 a simulation method, originally to study rock mechanics, known as Discrete Element Method (DEM). This technique takes into account the granular nature of the material by treating every grain as a distinct element (particle). Every particle interacts with the neighbors by means of contact and non-contact (body) forces, and can move translationally and rotationally. Newton's equations of motion describe the particles dynamics. Thereby, DEM simulations can provide dynamic information, such as trajectories of particles and transient forces acting on individual particles, which is extremely difficult to obtain by physical experimentation at this stage of development [15].

In contrast to the continuum methods, the discrete element method offers the advantage to have access to coordination number (number of contacting particles) and contact area of every grain. Continuum methods use phenomenological models that do not take into consideration the microstructure of the material [16], such as effects due to grain rearrangement, of local heterogeneities and anisotropy. As example, Figure 2.8 shows the particle mixing pattern induced by the

passage of a single bubble through two initially completely segregated layers of particles of different colors. For comparison issues, experimental data are presented in Figure 2.8 (a), discrete method in (b), and continuum method in (c). Differences in the distribution of density can be easily noted. The discrete model shows a good correspondence with the experimental observations, whereas the continuum model overpredicts the mixing [17].

In recent years, DEM has been rapidly extended to study several fields of engineering due to multiple efforts in the simulation technique and computational technology evolution. Examples of application are vibratory sphere packing [18], ball milling [19], sintering process [4], and even for fluidization, where DEM may be coupled with computational fluid dynamics [17]. A good review of DEM applications and findings has been done by Zhu et al. [15].

Figure 2.8: Mixing patterns of a colored under-layer of particles induced by a single bubble: (a) experiment; (b) discrete method; (c) continuum method [17].

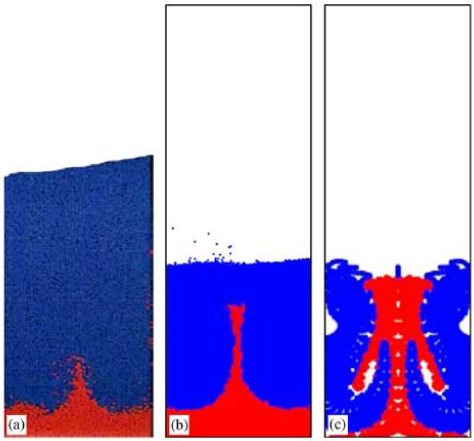

Application of DEM to simulate sintering in three-dimensional systems has become more frequent in the last decade. One of the first works, Martin et al. (2006) [4] have simulated the sintering of copper powder at varying temperatures and proposed a grain-coarsening scheme. Prior to sintering, the samples were compacted isostatically or uniaxially in order to analyze whether the compaction technique can influence the sintering behavior. They have found that uniaxially

compaction induces anisotropy in the sample during sintering. The simulations have shown a good accordance with the experimental data, mainly when coarsening scheme has been included.

Henrich et al. (2007) [3] have simulated free and pre-assisted solid-state sintering of powders with special attention to the grain rearrangements during sintering. The authors have described in details a method for generating a realistic initial configuration of particles. It has been found that the densification rate is enhanced by grain rearrangements, whereas bulk and shear viscosity are reduced. Grain rearrangement has also affected the crack formation. When a coefficient of friction has been included (imposing a resistance to the rearrangements), cracks have formed along the sample.

Such findings concerning evolution of cracks have been confirmed by Martin et al. (2009) [20]. The authors have investigated deeper the evolution of defects (cracks) during sintering in the unconstrained and constrained sample, with varying coefficient of friction between particles. The authors' main conclusion has been that it is necessary to have some form of constraint to nucleate and/or grow cracks. Defects may nucleate and grow from localized heterogeneities (at the length of few particles) and the green density can influence in the defect growth.

Wonisch et al. (2007) [21] have used DEM to study the stress-induced anisotropy through sintering of alumina samples. The authors have found that intergranular pores are preferentially orientated along the compressive loading axis in accordance with their experimental observation and with Martin et al.'s work [4].

The effect of particle size distribution on sintering has been studied by Wonisch et al. (2009) [22]. The authors have simulated samples with normal, lognormal and bi-modal size distribution, in which varying width distribution was used. The main finding has been that the densification rate declines when the distribution width increases, although particle rearrangement is enhanced.

The effect of a substrate on the sintering of films has been studied by Martin and Bordia (2009) [23]. The interaction between particles and substrate has been modelled by viscous drag (friction). Their work has shown that the substrate can induce heterogeneity and anisotropy along the film thickness in which was initially homogeneous and isotropic. The degree of anisotropy depends on the value of the viscosity at the interface.

Rasp et al. (2013) [24] has investigated the influence of varying initial coordination number but similar green densities on the sintering

behavior. Their simulations have shown that the densification is strongly retarded in the case of low initial coordination numbers.

Considering sintering of composites using DEM simulations, just few works can be found in literature. In the earliest works aimed in this topic, Jagota and Scherer (1993) [25, 26] have studied the sintering of monosized composites by varying the fraction of hard spheres and assuming that all contacts follow a linear viscous law. These authors have concluded that there is an inclusion fraction limit (hard spheres) above which the apparent viscosity of the packing increases drastically depending on the nature of the contact between inclusions.

Later on, Olmos et al. (2009) [5] have investigated the sintering of mono-sized copper/alumina composites by varying the volume fraction of alumina inclusions (between 5% and 30%) and compared with experimental data. Sintering has been carried out at temperature of 1000 °C, which is reasonable to treat alumina particles as hard spheres. The experiments have shown that the densification rate decreases as the fraction of inclusions increase. For the case of 30% alumina, the sample barely has sintered since inclusions can form a continuous network (percolation) above this solid volume content, which hinders sintering. Overall, the simulations have shown a good agreement with the experimental data.

Yan et al. (2013) [6] have investigated the effect of volume fraction, size and homogeneity (agglomerates) on the sintering behavior of ceramic/metal composites. Metal particles have been treated as soft spheres, and ceramic particles as hard spheres (sintering temperature at 800 °C). The authors, in accordance with Olmos et al. [5] and Jagota and Scherer [26], have found that the densification rate is reduced as the size of inclusions decrease. Furthermore, the simulations have shown that the densification rate decreases as inclusion size decrease for a given volume fraction. The same behavior has found for agglomerate of inclusions. The authors claim that agglomerates of fine inclusions may be considered as larger particles of agglomerated total size.

In such works of composites sintering, the authors have used models considering one of the materials as rigid inclusions. It means that just one material sinters and the other follows, for example, an elastic law. However, whether sintering is carried out at a high enough temperature, both materials can sinter and be treated as soft spheres.

2.5 MATHEMATICAL DESCRIPTION OF DEM

In the DEM scheme, the interactions of spherical particles are accounted by modeling the evolution of the packing as a dynamic process. The particles are described by their individual vectors: position $\vec{r}_i$, velocity $\vec{u}_i$ and angular velocity $\vec{\omega}_i$, and scalars: mass $\mathbf{m_i}$, moment of inertia $\mathbf{I}_i$, and radius $\mathbf{R}_i$. These vectors are shown in Figure 2.9, which represent two overlapped particles on a vectorial plane. This Figure represents the soft sphere approach in which the normal force $\vec{F}_n$ and the tangential force $\vec{F}_t$ can be observed. The overlap $\mathbf{h}$ between particles and the forces are discussed in the next chapter.

Figure 2.9: Two overlapped particles on a vectorial plane showing their vectors.

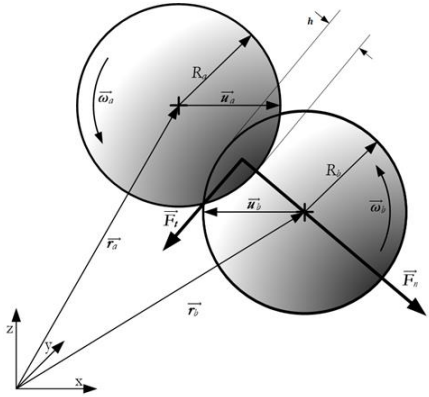

Figure 2.10 shows a flowchart that represents the DEM algorithm for the temporal evolution of the particles. As observed, in each simulation time step $\mathbf{\Delta t}$, firstly the number of neighbors in contact of every particle is determined (Figure 2.10 a), where the *Verlet-Neighbor List Method* [27, 28] may be used. A pair of particles is considered in contact if the distance between their centers is less than the sum of their radii. An example may be observed in Figure 2.9, where $|\vec{r}_b - \vec{r}_b| < \mathbf{R}_a + \mathbf{R}_b$, thus particles are considered in contact.

Figure 2.10: Flowchart representing the DEM algorithm.

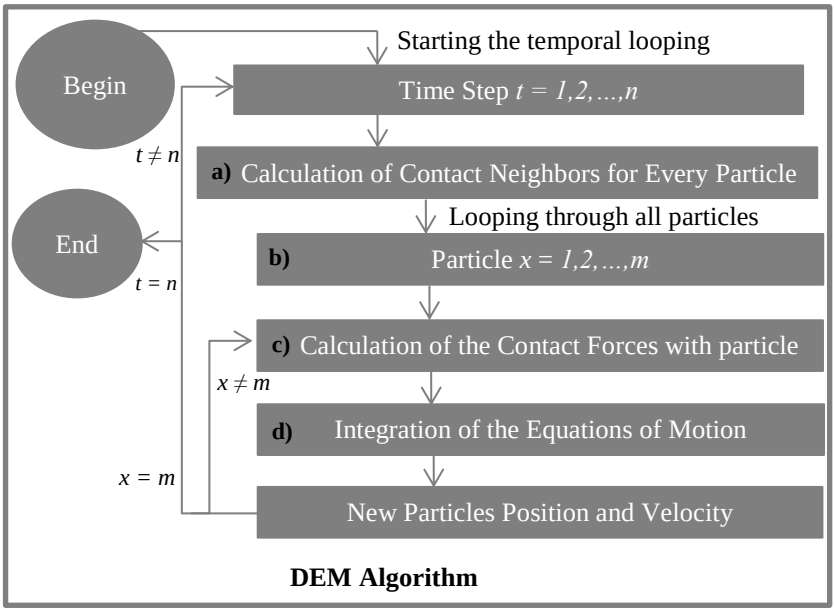

Then, after the neighborhood calculation, the algorithm goes through every particle (Figure 2.10 b). The forces between neighboring particles are calculated (c) depending on a given force law (these forces are described in the next section). With the total force acting on the particle and using the Newton's second law, it is possible to obtain the new velocity and position [3]. The time evolution of the particle positions is governed by Newton's equation of motion, which provides the balance of forces and moments, as follows:

$$\frac{d}{dt}\vec{r}_i = \vec{u}_i, \quad \mathrm{m}\frac{d}{dt}\vec{u}_i = \vec{F}_i^{tot} = \sum_{j \neq i} \vec{F}_{ij} \tag{2.3}$$

$$\mathrm{I}\frac{d}{dt}\vec{\omega}_i = \vec{T}_i^{tot} = \sum_{j \neq i} \vec{T}_{ij} \tag{2.4}$$

$\vec{F}_i^{tot}$ denotes the total force acting on the ***i***th particle, computed as the sum of all forces $\vec{F}_{ij}$, and $\vec{T}_i^{tot}$ the total torque acting on the ***i***th particle.

For the time integration of these equations of motion, the *Leapfrog Integration Method* [29] may be used (Figure 2.10 d):

$$\vec{r}_i(t+\Delta t) = \vec{r}_i(t) + \Delta t\ \vec{u}_{\mathrm{i}}(t) + \frac{1}{2m}(\Delta t)^2 \vec{F}_i^{tot} \quad (2.5)$$

$$\vec{u}_{\mathrm{i}}(t+\Delta t) = \vec{u}_{\mathrm{i}}(t) + \frac{1}{2m}\Delta t\ (\vec{F}_i^{tot}(t) + \vec{F}_i^{tot}(t+\Delta t)) \quad (2.6)$$

$$\vec{\omega}_i(t+\Delta t) = \vec{\omega}_i(t) + \frac{1}{2I}\Delta t\ (\vec{T}_i^{tot}(t) + \vec{T}_i^{tot}(t+\Delta t)) \quad (2.7)$$

2.6 CONTACT MODEL FOR SINTERING

DEM simulations need a mathematical model that describes properly the interaction forces between particles. Equation 2.8 shows the Newton's second law and forces that might act on ***i***th particle [30]:

$$\mathrm{m}\frac{d}{dt}\vec{u}_{\mathrm{i}} = \vec{F}_i^f + \vec{F}_i^g + \sum_{k\neq i}\vec{F}_{ik}^{nc} + \sum_{j\neq i}\vec{F}_{ij}^c \quad (2.8)$$

The force $\vec{F}_i^f$ results from the particle-fluid interaction, such as drag force or due to the pressure gradient. In solid-state sintering, this sort of force does not exist due to the absence of fluid. The term $\vec{F}_i^g$ represents gravitational forces acting on the particles. Even though gravity is present during sintering, most works do not consider its contribution [3, 4].

$\vec{F}_{ik}^{nc}$ results from the non-contact force acting on particle ***i***th by the interaction with particle ***k***th, such as the van der Waals or electrostatic forces. Van der Waals forces play an important role to keep the particles together in the green body, but do not affect the sintering behavior.

$\vec{F}_{ij}^c$ represents contact forces that result when particle ***i***th is physically contacting particle ***k***th. Examples of contact forces include frictional forces, spring force and air resistance force. In DEM modelling, this sort of forces acts on the point of contact between two particles. Figure 2.11 shows a representation of two soft particles interacting with an overlap **h** and such point of contact is shown by the dotted line.

In sintering, as discussed in the previous chapter, the mass transfer for neck formation and densification only takes place at the

contacts of particles. Hence, a contact model that predicts realistically the sintering behavior is necessary.

Figure 2.11: Contact geometry between two overlapped particles.

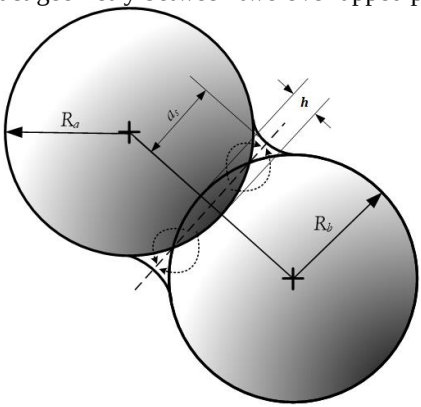

In this work, whose purpose is to simulate sintering of composites, a special approach is proposed based on Bouvard and McMeeking's model [31] and the observations of Olmos et al. [5]. The metal material is nickel (Ni) and the ceramic one is alumina (Al_2O_3). Three types of contacts coexist through the samples and are treated in a different way (see Figure 2.12):

- between metal particles (Ni-Ni);
- between ceramic particles (Al_2O_3-Al_2O_3);
- between metal and ceramic particle (Ni-Al_2O_3).

Figure 2.12: Contact geometry between two overlapped particles.

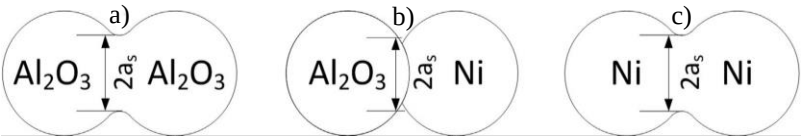

The three contacts have two different behaviors. Briefly, the Ni-Ni and Al_2O_3-Al_2O_3 contacts are the sintering ones (Figure 2.12 a) and c)), described by a sintering-viscous model. The Ni-Al_2O_3 is a non-sintering contact (Figure 2.12 b) and follows a viscous model (described in details as follows).

The contact model for sintering is based on Bouvard and McMeeking's model [31], which considers grain boundary and surface diffusion as the main mechanisms of mass transport. As the simulations are carried out with a constant temperature $\boldsymbol{T}$, the diffusion coefficient for vacancy transport in the grain-boundary with thickness $\boldsymbol{\delta_b}$ is described by Equation 2.9. $\boldsymbol{Q_b}$ is the activation energy, $\boldsymbol{R_g}$ the ideal gas constant and $\boldsymbol{D_{0b}}$ pre-exponential factor. Diffusion coefficient is used to calculate the diffusion parameter (Equation 2.10), where $\boldsymbol{\Omega}$ is the atomic volume and $\boldsymbol{k}$ the Boltzmann constant.

$$\boldsymbol{D_b = D_{0b}\exp\left(\frac{-Q_b}{R_g T}\right)} \tag{2.9}$$

$$\Delta_b = \frac{\boldsymbol{\Omega}}{\boldsymbol{kT}}\,\boldsymbol{\delta_b D_b} \tag{2.10}$$

As the simulations are carried out at 1220 °C, metal-metal and ceramic-ceramic contacts are sintering. For such a case, given a system of two particles of identical radius **R**, and an overlap **h**, the normal force $\vec{\boldsymbol{F}}_n$ (see Figure 2.9) acting at the contact is described by:

$$\vec{\boldsymbol{F}}_n = \frac{\boldsymbol{\pi a_s^4}}{\boldsymbol{2\beta}\Delta_{b,m}}\,\vec{\boldsymbol{u}}_{\boldsymbol{rel,n}} - \vec{\boldsymbol{\imath}}_{\boldsymbol{n}}\frac{\boldsymbol{\alpha}}{\boldsymbol{\beta}}\boldsymbol{\pi R\gamma_{s,m}} \tag{2.11}$$

where $\boldsymbol{\gamma_{s,m}}$ is the surface energy and $\Delta_{\boldsymbol{b,m}}$ diffusion parameter of the material, depending on which kind of contact is taking place. Contact radius $\boldsymbol{a_s}$ can be observed in Figure 2.11.

The first term on the right-hand side of Equation 2.11 may be considered as a normal resistance that opposes the movement. Its value can be either compressive or tensile, depending on the particle-particle relative velocity in the normal direction $\vec{\boldsymbol{u}}_{\boldsymbol{rel,n}}$. The second term relates to a sintering tensile force due to the surface energy $\boldsymbol{\gamma_s}$. The vector $\vec{\boldsymbol{\imath}}_{\boldsymbol{n}}$ is the unit vector in the normal direction to the contact area between two particles. This vector is necessary to convert the sintering term from a scalar into a vector. Note that the viscous term depends on the size of the contact radius $\boldsymbol{a_s}$ to the power of four, thus leading to very large resistance for large overlaps [20].

The parameters $\boldsymbol{\alpha}$ and $\boldsymbol{\beta}$ depend on the ratio of the grain-boundary $\boldsymbol{\delta_b D_b}$ diffusion to the surface diffusion $\boldsymbol{\delta_s D_s}$ [23], in the following relation:

$$\boldsymbol{\varphi = \frac{\delta_b D_b}{\delta_s D_s}} \tag{2.12}$$

where for a pair of particles $\boldsymbol{\beta = 4}$ may be used for all values of $\boldsymbol{\varphi}$. The parameter $\boldsymbol{\alpha = 9/2}$ is used for $\boldsymbol{\varphi = 2}$, $\boldsymbol{\alpha = 3}$ for $\boldsymbol{\varphi = 0.2}$, and $\boldsymbol{\alpha = 5/2}$ for $\boldsymbol{\varphi = 0.02}$. In other words, it is possible to choose which mechanism would be the dominant throughout the simulation only changing the parameter $\boldsymbol{\alpha}$. As grain boundary diffusion is the most important mechanism to promote densification during sintering (see Section 2.3.4), it was chosen $\boldsymbol{\varphi = 2}$ (grain boundary twice more influent then surface diffusion). Then, in the present work the used parameters are $\boldsymbol{\alpha = 9/2}$ and $\boldsymbol{\beta = 4}$.

The tangential contact force $\vec{\boldsymbol{F}}_{\boldsymbol{t}}$ represents a viscous resistance against sliding and opposes the particle-particle relative velocity in the tangential direction $\vec{\boldsymbol{u}}_{\boldsymbol{rel,t}}$, is given by [32, 33]:

$$\vec{\boldsymbol{F}}_{\boldsymbol{t}} = -\boldsymbol{\eta_{part}} \frac{\boldsymbol{\pi a_s^2 R^2}}{\boldsymbol{2\beta \Delta_{b,m}}} \vec{\boldsymbol{u}}_{\boldsymbol{rel,t}} \tag{2.13}$$

where $\boldsymbol{\eta_{part}}$ is a viscous parameter with no dimension. This coefficient can be considered as a friction parameter for the sliding of particles, where surface rugosity and shape of the particles may affect its value. Even though its value is difficult to quantify experimentally, it has been shown to be of primary importance for the macro defect initiation [20]. Martin and Bordia [23] suggest that the value of the viscosity $\boldsymbol{\eta_{part}}$ should be <1, because the normal viscosity term in Equation 2.11 should be of the same order or larger than the tangential viscosity term (Equation 2.13) when the normal and tangential relative velocities are of the same order. Martin et al. [20] have investigated different values of the viscosity parameter. They have found that for $\boldsymbol{\eta_{part} > 0.01}$, the rearrangements of particles are very restrict and crack formation can occur along the sample even without preexisting defects. For $\boldsymbol{\eta_{part} = 0.01}$, sintering has taken place with heterogeneous densification and without formation of large cracks. This value, as an intermediary value of viscosity, is used in this work.

The contact radius $\boldsymbol{a_s}$ is calculated by Coble's model [34]:

$$\boldsymbol{a_s{}^2 = 2Rh} \tag{2.14}$$

which is dependent of the overlap $\mathbf{h}$ between the particles. It is important to point out that Coble's model considers the mass transfer to the growing of the neck when two particles are approaching and overlapping each other. In other words, the contact radius $\boldsymbol{a_s}$ calculated takes into account the conservation of mass, as represented in Figure 2.11.

For the contact between metal-ceramic (Ni-Al_2O_3), it is considered that no sintering takes place. The normal force for them has been adapted by the observations of Olmos et al. [5]. The authors have studied experimentally the sintering with a mixture of copper and alumina. One of their results is that during sintering, at temperatures typical for the metal phase but not sufficient for alumina, the metal particles exhibit viscous deformation in the contact region to an alumina particle. The shape of the contact region is, thereby, comparable to a sintering neck. To consider this viscous effect at the Ni-Al_2O_3 contacts, the normal force is given solely by the viscous term in Equation 2.11, resulting in:

$$\vec{\boldsymbol{F}}_{\boldsymbol{n}} = \frac{\boldsymbol{\pi a_s^4}}{\boldsymbol{2\beta\Delta_{b,m}}}\,\vec{\boldsymbol{u}}_{\boldsymbol{rel,n}} \tag{2.15}$$

where $\Delta_{\boldsymbol{b,m}}$ is calculated from the mean value between ceramic and metal diffusion parameters.

Friction is also considered in metal-ceramic contacts and is calculated by the tangential force in Equation 2.13, where $\boldsymbol{\eta_{part} = 0.01}$ as well.

In order to study the effect of varying size of particles in the packing, samples with bimodal packings were generated and an equivalent radius $\mathbf{R}^*$ is defined between two particles of radius $\mathbf{R_1}$ and $\mathbf{R_2}$ [23]:

$$\mathbf{R}^* = \frac{\mathbf{2R_1R_2}}{\mathbf{(R_1+R_2)}} \tag{2.16}$$

where $\mathbf{R}$ in Equation 2.11 and 2.13 can be replaced by $\mathbf{R}^*$. Many authors [20, 22] have used this generalization, which has its origin in elasticity and plasticity theory. Moreover, this is in good quantitative agreement with numerical simulations carried out by Pan et al.[35] and Parhami et al. [36] on sintering behavior of two-spheres systems with size ratio of up to four.

3 SIMULATION AND ANALYSIS METHODS

As first part of this project, this chapter presents the adjustments and developments done on the software MUSEN [37] in order to enable it to simulate sintering. The topics include a short description of the software MUSEN, the main assumptions for sintering, the validation of the sintering behavior with a system of two particles and a method proposed to calculate the density evolution.

3.1 SOFTWARE MUSEN

Software MUSEN, developed by Dosta [37, 38], is a Graphical User Interface (GUI) with implemented DEM equations, which can be used to simulate the sintering process with some adjustments.

The MUSEN system has an algorithm that generates packing of particles with random distribution. The algorithm produces packings inside the simulation box, which is defined as a three dimensional space with a specified geometry (cubic, spherical or cylindrical) where periodic boundary conditions could be implemented to act on their borders. The algorithm to fill the simulation box is a dynamic method and works basically in three steps. Firstly, the number of particles is calculated from the porosity required and the simulation box's volume. Secondly, this amount of particles is filled into the box occupying random sites and a small overlap is allowed between particles. Thirdly, the particles are displaced on a dynamic way, in order to attain a better arrangement of the particles and reduce the overlap between them. Then, it is possible to manipulate the packing, for example to delete particles or change their positions.

A mathematical model for diverse purposes can be implemented in the language C++ and loaded into the software. Different material properties may be loaded and used for simulations. As output data, the software provides a txt file with the particle's vectors position, velocity and force for each saved time step. On the graphical interface, the behavior of the sample throughout the time can be observed in such a way that it allows observing crack formation, rearrangement of particles and densification.

The features previously described are just some of the available tools in the software. Moreover, new developments and adjustments can be done in order to improve the software capabilities. To enable the sintering simulation, the main adjustments developed for this project

have been the calculation of the coordination number (CN) (number of neighboring particle in contact with each particle), the average contact radius (ACR) evolution and the density evolution. For this purpose, it has been developed an algorithm in Matlab® which reads the output txt file with the particle vectors along the simulation provided by the software and calculates the CN and the ACR evolution throughout the simulation. In addition, the particles can be colored by the coordination number on the graphical interface. For the densification calculation, a new method has been developed and implemented into the software, as described in details in the next section.

Figure 3.1 shows a chart resuming the input and output data (mostly related to the sintering parameters) of software MUSEN. The DEM algorithm (gray part) refers to the algorithm described in Section 2.5 (Figure 2.9). Figure 3.2 shows a screenshot of MUSEN's interface with a packing of copper particles. As is observed in this figure, the software allows coloring particles by different characteristics, such as velocities, angular velocity, diameter, material and coordination number.

Figure 3.1: Diagram showing the Software MUSEN's input and output data.

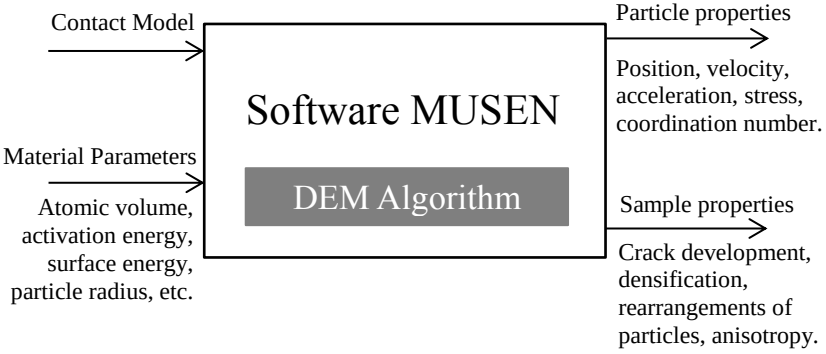

Figure 3.2: Screenshot of Software MUSEN's interface with a spherical packing of copper particles.

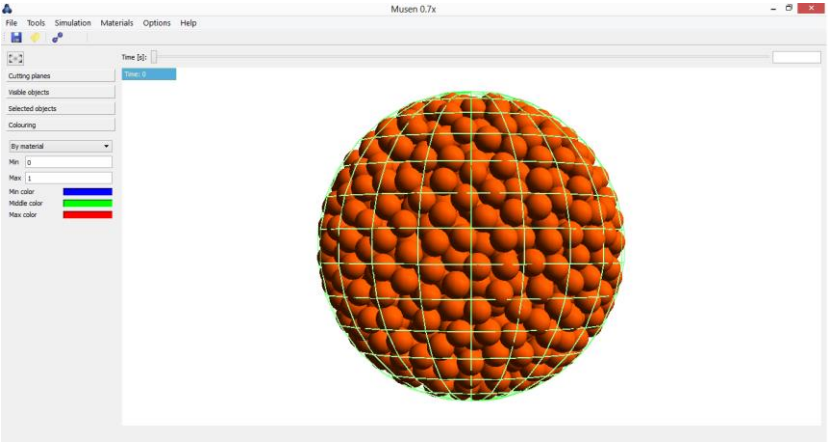

3.2 ASSUMPTIONS FOR THE SINTERING SIMULATION

The first part of this project consisted to define the basic assumptions to simulate the sintering process. As any simulation work, it is important that the assumptions simplify the problem but, at the same time, do not affect the physical reality of the process.

For sintering, a usual assumption mentioned in many works [4, 5] is to neglect the rotational motions of the particles. Martin et al. [39] have stated that the rotational motions can be neglected for packings with particle coordination number between 6 and 10. Such a value of CN is found in the sintering packings since its relative density is about 64%. Thus, the torque and angular velocity calculation (Equations 2.4 and 2.7) are deactivated in the software MUSEN during sintering simulation.

Software MUSEN allows generating packings with typical relative density of green body from 55% to 64%. Hence, it is not necessary to compact the sample and the sintering simulation can be carried out as soon as the packing is generated. Furthermore, the simulations have been performed at sintering constant temperature of 1220 °C.

Grain growth is not considered in this work because the model used (see Section 2.6) does not predict such behavior. For this reason, the authors of most works [22, 23] have stopped their simulations at

relative density of 0.90; for that grain growth has a limited influence on the process. In addition, a basic assumption of DEM simulations is that two neighboring contacts of one particle must not interact. Figure 3.3 represents such situation, where particles A and C start to interact after some simulation time due to the large overlaps developed with particle B. In other words, when the overlap between two particles attains a certain maximum value, the simulation is not valid anymore. This maximum value of overlap also corresponds at relative density about 0.90. Those authors have used such limiting relative density because they have simulated only one material with one densification kinetics. It means that all overlaps (and the contact radius) between particles follow the same kinetic.

Figure 3.3: Representation of two neighboring particles interacting.

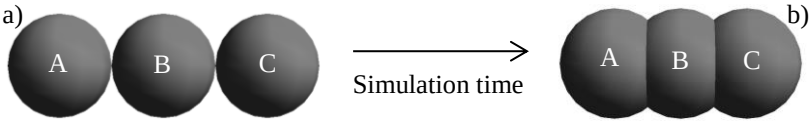

However, for this work in which two materials with two different kinetics are used, the limitation must be related to the contact radius evolution between these two phases (nickel-nickel contact and alumina-alumina contact) instead to the relative density. In order to find out at which average contact radius the simulations should be stopped, a calibration has been done relating the normalized average contact radius to the relative density evolution as shown in Figure 3.4.

The contact radius has been normalized by the particle radius to be independent of the particle size. As observed, the normalized average contact radius that corresponds to relative density of 0.90 is equal to 0.65. Therefore, the limiting normalized contact radius is 0.65 and the simulation must be stopped at this point. It is important to point out that this evolution is neither dependent on the material nor on the number of particles in the simulation box. It is essentially a geometric evolution and then can be used for both alumina-alumina and nickel-nickel contacts.

Figure 3.4: Evolution of the normalized average contact radius as function of the relative density.

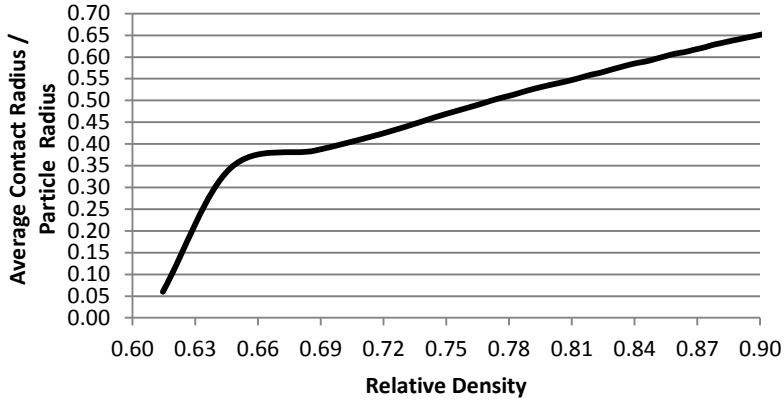

3.3 NUMERICAL EXAMPLE WITH A TWO-PARTICLE SYSTEM

In order to investigate the correct behavior of the calculations provided by the software MUSEN according to the used contact model, Figure 3.5 shows a numerical example with two particles of radius 0.05 μm before simulation (a) and after 60 seconds of simulation (b) at temperature of 1200 °C. For such example, typical alumina parameters [20] have been used and the time step equal to 10^{-4} s. Table 3.1 shows all simulation parameters for this example. It should be pointed out that the contact diameter shown in Figure 3.5 (b) (white arrow) is not the contact diameter used for the calculations. Instead of that, it is used the contact diameter given by Equation 2.14 (contact radius), which considers the conservation of mass during the process.

Table 3.1: Simulation and alumina parameters for the numerical example.

Parameter	Symbol	Unit	Value
Density	ρ_m	kg/m³	3950
Atomic volume	Ω	m³	8.47×10^{-30}
Surface energy	γ_s	J/m²	1.1
Grain boundary thickness times diffusion parameter	$\delta_b D_{0b}$	m³/s	1.3×10^{-8}
Activation energy	Q_b	kJ/mol	475
Temperature	T	°C	1200
Particle radius	R	µm	0.05
Time step	Δt	s	1×10^{-4}

Source: Martin et al. (2009) [20].

As simulation proceeds (Figure 3.5), some parameters of the two particles change (Figures 3.6 and 3.7). Figure 3.6 (a) shows the forces evolution, and Figure 3.6 (b) shows the evolution of the relative velocity in normal direction. As expected from Equation 2.11, in Figure 3.6 (a) the sintering force presents a constant value through the entire simulation, whereas the viscous force presents a more complex behavior. As discussed previously, this latter force is dependent on the relative velocity in the normal direction $\boldsymbol{u_{rel,n}}$ and, since the particles are initially stopped, it starts from zero. The curve of velocity in Figure 3.6 (b) presents a similar behavior of the viscous force in (a).

Figure 3.5: Representation of two alumina particles before simulation (a) and after 60 s of simulation (b).

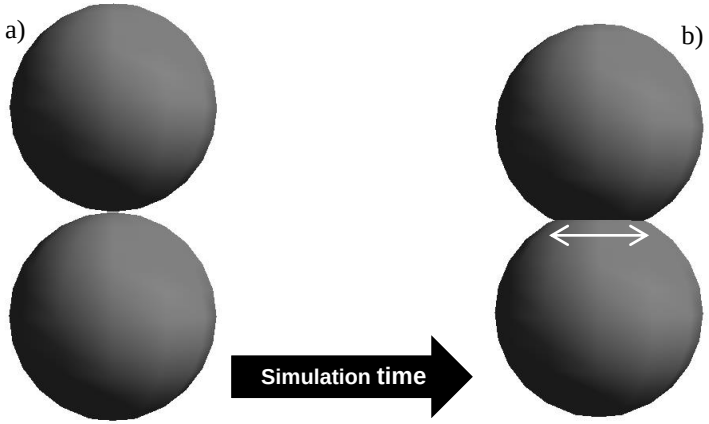

To explain such behavior, it is necessary to analyze Equation 2.11. In the first time step, since viscous force is zero, the only force acting on the particles is the tensile sintering force. Hence, there is a large total force attracting the particle, leading the development of high velocities for the next time step. Then, such high velocities results in a great increase of the viscous force. On the other hand, the viscous force developed will offer a resistance to the motion of the particles, which ends up decreasing the velocities. In other words, the viscous force induces influences and simultaneously it is influenced by the particle velocities. This explanation may be supported by observing Figure 3.6 (b), where the relative velocity attains a maximum velocity at the same time when the viscous force is maximum in (a). Moreover, it is observed that the velocity does reach neither a constant value nor zero. For this reason, it can be considered that the particles attain a 'virtual' equilibrium.

Figure 3.7 (a) shows the displacement of the particles as simulation goes on and (b) shows the evolution of the contact radius between the particles. A great part of the total displacement occurs in the beginning of the simulation, when the particles velocity is higher as it was in Figure 3.6 (b).

In Figure 3.7 (b), contact radius rises nearly similar to the displacement and it is in accordance with Coble's model in Equation 2.14.

Figure 3.6: The evolution of sintering and viscous force (a) and relative velocity in the normal direction (b) of the pair of particles as simulation proceeds.

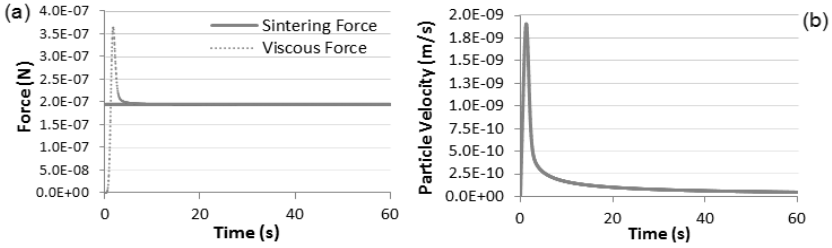

These results in Figures 3.6 and 3.7 are quite similar to those obtained by Nosewicz et al. [16], where the graphs of force, velocity and displacement have shown basically the same trend. Since the authors

have used the same contact model, it is a proof that the implementation of the contact model in the system has been done successfully.

Figure 3.7: The evolution of the displacement (a) and contact radius (b) of the pair of particles as simulation proceeds.

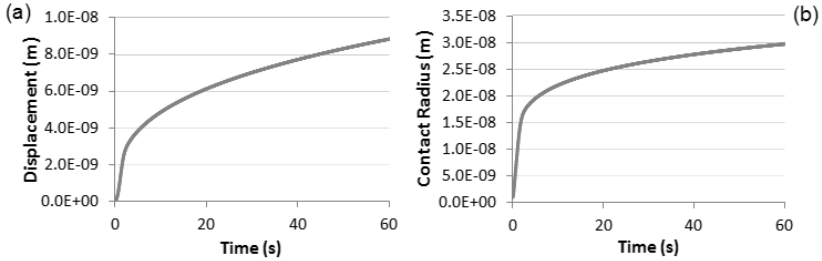

3.4 DENSIFICATION CALCULATION THROUGHOUT THE SIMULATION

Sintering process is also known as a densification process. Thus, it is extremely important to know how the evolution of the relative density occurs as simulation proceeds. For this reason, a method has been developed to calculate the densification curve throughout the simulation.

Density $\boldsymbol{\rho}$ is defined by $\frac{\boldsymbol{m}}{\boldsymbol{V}}$, where $\boldsymbol{m}$ is mass and $\boldsymbol{V}$ is volume. For a particulate system, the relative density $\boldsymbol{\rho_v}$ of a specific volume $\boldsymbol{V_s}$ may be calculated by the following equation:

$$\rho_v = N_p \frac{\rho_m V_p}{V_s} \tag{3.1}$$

where $\boldsymbol{N_p}$ is the number of particles inside the volume, $\boldsymbol{\rho_m}$ is the material density of the particles and $\boldsymbol{V_p}$ is the volume of each particle. The great difficulty of this approach is to calculate the exact volume $\boldsymbol{V_s}$ of the system, since during sintering simulation the particles can move in an inordinate way due to the heterogeneities of random packings. Furthermore, symmetry is not present in many kinds of studied systems.

To solve this problem, an alternative has been proposed as follows. First of all, a spherical volume $\boldsymbol{V_s}$ with radius $\boldsymbol{R_V}$ and position vector $\boldsymbol{r_V}$ is defined, where the density will be calculated. Figure 3.8 (a) shows a cubic packing of particles generated by the software, whereas

(b) is the same cube but cut in the central plane (the particles are hidden) and such spherical volume $\boldsymbol{V_s}$ can be seen with the gray lines.

Secondly, an algorithm goes through every particle ***i*th** in the system with a radius $\boldsymbol{R_i}$ and position vector $\boldsymbol{r_i}$ and checks whether the particle is inside, outside or within the border of the spherical volume. For the calculation, the following geometrical cases must be considered:

Case 1) particle is outside the sphere: $|r_v - r_i| \geq R_v + R_i$

Case 2) particle is inside the sphere: $|r_v - r_i| + R_i \leq R_v$

Case 3) particle is within the border and:

Case 3.1) particle's center outside the border:

$$R_v < |r_v - r_i| < R_v + R_i$$

Case 3.2) particle's center inside the border:

$$R_v - R_i < |r_v - r_i| < R_v$$

Figure 3.8: Random cubic packing of particles (a) and the same sample but cut in the central plane and with a spherical volume defined by the gray lines where the density is calculated (b).

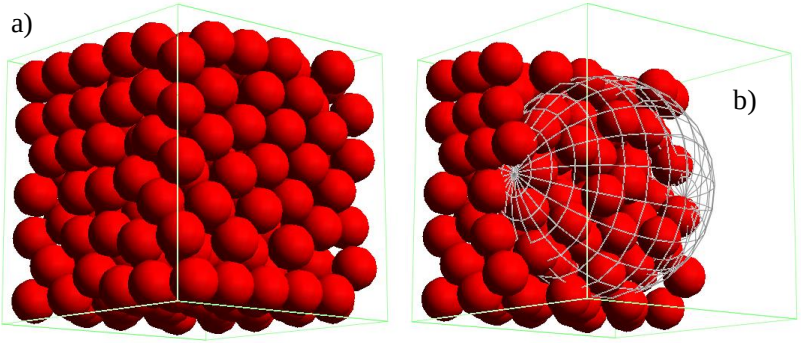

Case (1) and case (2) are more trivial to be solved. In case (1), the particle is not considered. In case (2) the total volume of the particle is taken into account for the density calculation. Case (3) is more complex to deal with because the particle's partial volume inside the spherical volume must be calculated. For such a case, a solution regarding the intersection between two spheres has been used. Figure 3.9 represents the spherical cap with height $\boldsymbol{h}$ of a sphere with radius $\boldsymbol{r}$. The volume of the spherical cap is given by:

$$V_{cap} = \frac{\pi h^2}{3}(3r - h) \tag{3.2}$$

Figure 3.10 (a) shows the case (3.1), where the particle's center is outside of the spherical volume. The partial volume inside the spherical volume is the sum of the orange and green volumes. The volume of the green part is calculated as a cap of the big sphere with height $\boldsymbol{h}$, whereas orange part is calculated as a cap the small sphere with height $\boldsymbol{H}$.

Figure 3.9: Representation of spherical cap.

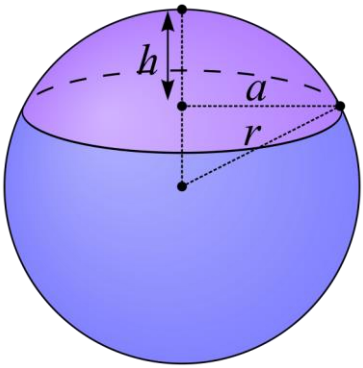

Then, the partial volume inside the spherical volume for the case (3.1) is given by:

$$V_{partial} = V_{capGreen} + V_{capOrange} \tag{3.3}$$

Figure 3.10 (b) shows the case (3.2), where the particle's center is inside of the spherical volume. The partial volume inside the spherical volume is calculated slightly different. The volume (blue + yellow) $\boldsymbol{V_{capYB}}$ is calculated as a cap of the small particle with a height $(\boldsymbol{h} + \boldsymbol{H})$. The volume of the yellow $\boldsymbol{V_{capY}}$ part is calculated as a cap of the big sphere with height $\boldsymbol{h}$.

Figure 3.10: Representation of two overlapped spheres with the smallest particle's center outside the border (a) and inside the border (b).

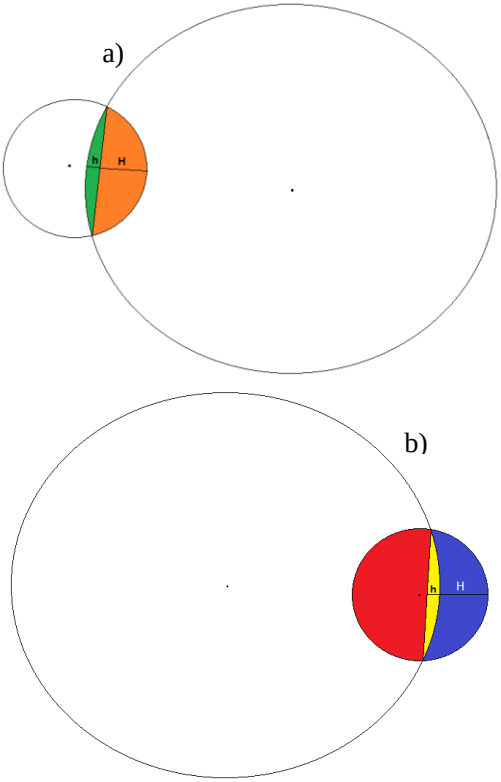

Then, the partial volume inside the spherical volume for the case (3.2) is given by:

$$V_{partial} = V_{total} - V_{capYB} + V_{capY} \tag{3.4}$$

where $\boldsymbol{V_{total}}$ is the total volume of the small particle.

Thereby, the partial volumes can be calculated and the density $\boldsymbol{\rho_v}$ in such spherical volume $\boldsymbol{V_s}$ is given by:

$$\rho_v = \rho_{material} \frac{\left[\left(N_p V_p\right)_{inside} + \sum_i V^i_{partial}\right]}{V_s} \tag{3.5}$$

where $\boldsymbol{N_p}$ is the number of particles entirely inside of the spherical volume, $\boldsymbol{V_p}$ is the total volume of one particle and $\boldsymbol{V^i_{partial}}$ is the partial volume of every particle ***i*th** that is within the border of the spherical volume.

Figure 3.11 shows an example of the relative density evolution of a cubic packing of alumina particles calculated by the procedure previously described. The behavior of this densification curve is quite similar to the theoretical curve showed in Figure 2.6 (Section 2.3.3) and it is a confirmation that the developed method calculates the densification correctly.

Figure 3.11: Relative density evolution over time of a cubic packing filled by alumina particles.

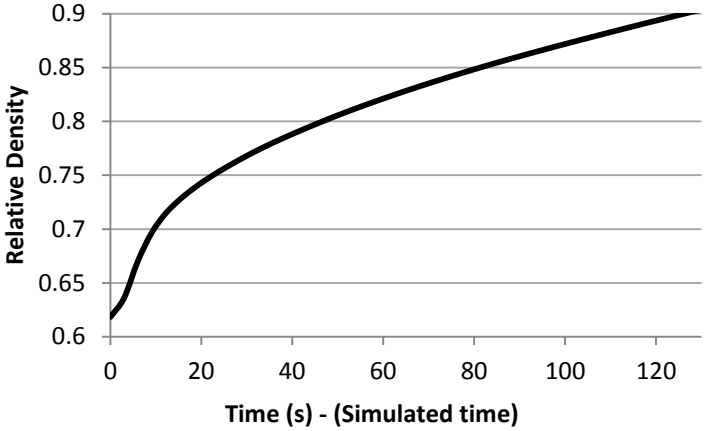

4 EXPERIMENTAL PROCEDURE

Before proceeding with the simulations, the packing of particles shall be generated and it should match some initial criteria: homogeneous and isotropic random packing of spheres, realistic coordination number and relative density for a green body.

The numerical samples for this work have been generated by the software MUSEN's algorithm of packing generation (see Section 3.1), which produces samples that satisfy the previous requirements. For all samples, a simulation box with a spherical geometry has been chosen, and the particles are randomly distributed through the packing. The maximum number of particles has been established to about 4000 particles. Unfortunately, a limitation of DEM is the number of particles simulated, which could lead to a prohibitive computational time. However, Henrich et al. [3] have stated that few thousands of particles are enough to have a good compromise between acceptable computing time and reliable results.

A common configuration used in DEM works are *the periodic boundary conditions* on the simulation box. This configuration allows an infinite lateral length to be represented, in which a particle that reaches the boundary of the simulation box will interact with the particle on the opposite side. However, due to the complexity of this configuration, it has not been implemented for the presented simulations. Thereby, a few simulations with a larger number of particles in the sample have been carried out in order to proof that the lack of periodic boundary conditions do not affect the overall results.

4.1 NUMERICAL SAMPLES

The numerical samples are divided into two groups:

- monosized packing;
- bimodal packing.

The monosized packings have been generated in order to investigate the influence of varying volume fractions of each material (alumina and nickel) on the sintering behavior. Thus, eight numerical samples with particle diameter of 100 nm have been produced with varying compositions. Table 4.1 describes these samples. Packings composed by pure alumina and pure nickel have been also produced to be used as reference. There are three kinds of structures among the samples and

they are shown in the last column: matrix system (pure material), matrix-particulate system and interpenetrating structures. The initial relative density of these packings is equal to 0.62. This relative density is below the random close packing limit of 0.64 [22] and it is a typical value for initial relative density used in DEM simulation of sintering [3, 4]. Figure 4.1 (a) shows a screenshots of the initial spherical packing generated by software MUSEN with 80% of nickel volume fraction and (b) shows the numerical sample with nickel volume fraction of 40%. Note that blue particles represent alumina and gray represent nickel.

Table 4.1: Data of monosized samples representing alumina and nickel composite.

Sample	Volume Fraction Nickel (%)	Volume Fraction Alumina (%)	Particle diameter (nm)	Number of Particles	Kind of Structure
100%	100	0	100	3987	Matrix (pure metal)
90%	90	10	100	3987	Matrix-Particulate
80%	80	20	100	3987	Matrix-Particulate
60%	60	40	100	3987	Interpenetrating
40%	40	60	100	3987	Interpenetrating
20%	20	80	100	3987	Matrix-Particulate
10%	10	90	100	3987	Matrix-Particulate
0%	0	100	100	3987	Matrix (pure ceramic)

Figure 4.1: Screenshot of numerical sample with nickel volume fraction of 80% (a) and 40% (b) generated by software MUSEN.

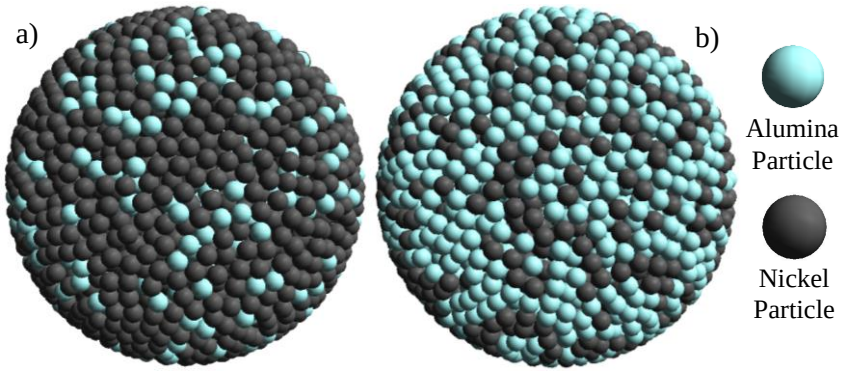

Table 4.2 describes the data of the monosized samples with higher number of particles. Note that the number of particles is four times higher than the smaller samples. The rest of the parameters, including particle size and volume fraction, are the same as the smaller samples.

Table 4.2: Data of monosized samples with higher number of particles representing metal-ceramic composite.

Sample	Volume Fraction Nickel (%)	Volume Fraction Alumina (%)	Particle diameter (nm)	Number of Particles
100%	100	0	100	16189
90%	90	10	100	16189
80%	80	20	100	16189
60%	60	40	100	16189
40%	40	60	100	16189
20%	20	80	100	16189
10%	10	90	100	16189
0%	0	100	100	16189

Figure 4.2: Screenshot of monosized samples with higher number of particles with nickel volume fraction of 80% (a) and 40% (b) generated by software MUSEN.

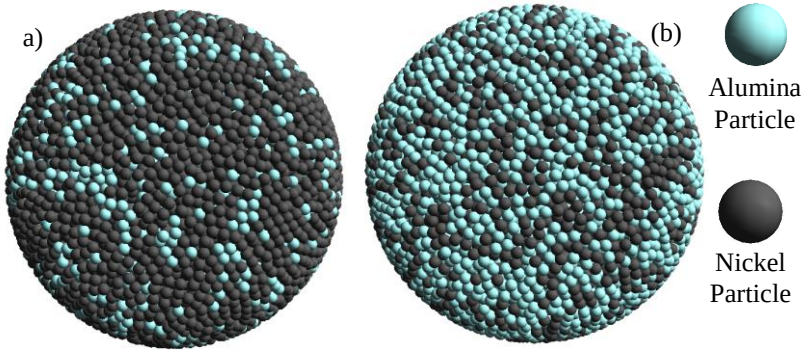

In order to investigate the influence of larger nickel particles during sintering, four numerical samples have been generated with varying nickel particles diameter. Table 4.3 shows the data related to the bimodal numerical samples. At this time, the nickel volume fraction of

60% and alumina particles diameter of 100 nm have been kept constant for all samples. The spherical simulation box size has been also kept constant. Hence, the total number of particles reduces as the nickel particle diameter increases. In fact, the number of nickel particles reduces, since the nickel particles increased their diameter.

Wonisch et al. [22] state that the maximum value of relative density attainable for the random packing of particles is higher when packing with different particle sizes is used. For this reason, the initial relative density increases slightly as the particle diameter increases. Figure 4.3 (a) shows a screenshot of the initial spherical packing generated by MUSEN with nickel particle diameter 1.5 times larger, and (b) shows the numerical sample with nickel particle diameter 3.0 times larger.

Table 4.3: Data of bimodal samples representing alumina and nickel composite.

Sample	Nickel Particles Diameter (nm)	Number of Nickel Particles	Number of Alumina Particles	Total Number of Particles	Relative Density
Reference	100	2392	1595	3987	0.625
1.5	150	734	1636	2371	0.635
2.0	200	310	1632	1942	0.652
2.5	250	160	1617	1777	0.660
3.0	300	92	1639	1731	0.660

Figure 4.3: Screenshot of numerical sample with nickel particle diameter 1.5 (a) and 3.0 times larger (b) generated by software MUSEN.

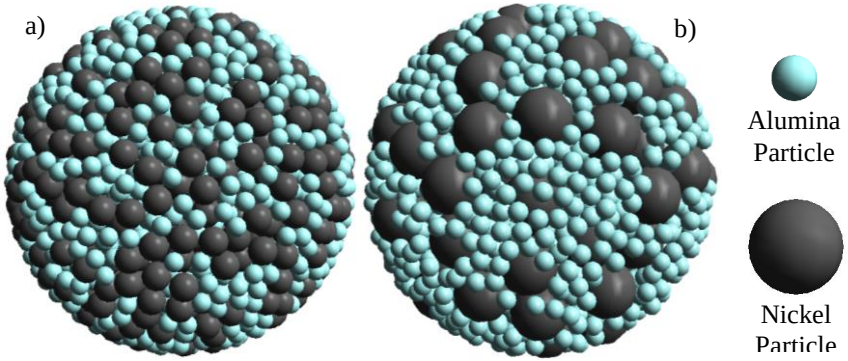

4.2 SIMULATION PARAMETERS

To simulate the sintering process for composites properly, real physical parameters for the materials chosen must be used. The metallic material chosen for this work was nickel, whereas the ceramic one was alumina. These materials have been chosen because their physical parameters are available in literature [5, 20] and, in fact, it is not easy to obtain them experimentally. Parameters such as activation energy for grain-boundary diffusion would need methods more complex to calculate them, for example quantum mechanism. The estimation of these parameters is out of scope of this project.

Table 4.4 lists the physical parameters [5, 20] for both materials required by the contact model used (Equations 2.9; 2.10; 2.11 and 2.13).

Table 4.4: Physical parameters for nickel and alumina used in the simulations.

Parameter	Symbol	Nickel	Alumina	Unit
Melting point	T_m	1455	2072	°C
Density	ρ_m	8912	3950	kg/m³
Atomic volume	Ω	1.18×10^{-29}	8.47×10^{-30}	m³
Surface energy	γ_s	1.72	1.1	J/m²
Grain boundary thickness times diffusion parameter	$\delta_b D_{0b}$	5.12×10^{-15}	1.3×10^{-8}	m³/s
Activation energy	Q_b	105	475	kJ/mol

Source: Martin et al. (2009) [20] and Olmos et al. (2009) [5].

The simulations have been carried out at constant sintering temperature. For the present work, the temperature has been chosen at 1220 °C. Nickel and alumina particles in this size can sinter at this temperature, even though nickel has a higher potential to sinter whether compared to alumina. This conclusion may be justified at Table 4.4, because the nickel melting point is lower than alumina. It leads to a better atomic motion for nickel at the sintering temperature (diffusion parameter; see Equation 2.9 and 2.10). Moreover, nickel has a higher value of surface energy that results in larger values for sintering force in Equation 2.11.

Table 4.5 lists other parameters related to the simulation, such as time step, saving time step and sliding friction coefficient (discussed in Section 2.5, Equation 2.13).

Table 4.5: Simulation parameters chosen for this work.

Parameter	Symbol	Unit	Value
Sliding friction coefficient (tangential force)	η_{part}	-	0.01
Temperature	T	°C	1220
Time step	Δt	s	1×10^{-7}
Saving time step	t_{save}	s	1×10^{-2}

5 RESULTS AND DISCUSSION

In this chapter we present the main results obtained along this project, as well as their interpretation. The results are divided into three parts. In the first part we show the simulations results of the monosized packing samples. Secondly, the results of the bimodal packings are exposed. The third part consists in a short presentation of the results with packings of larger number of particles.

5.1 MONOSIZED PACKINGS[1]

In this section we present and discuss the results about the simulations of the monosized packings with the varying contents of nickel and alumina. Firstly, it is presented the average contact radius evolution of the three kinds of contacts (nickel-nickel, alumina-alumina and nickel-alumina). Then, the average coordination number evolution is presented for the three kinds of contacts. Lastly, the global densification curves of all samples are shown and discussed. In order to clarify and support some explanations given along this section, some images of the samples after the simulation are also exhibited.

Before starting to present the results, it is important to recall the concept of *interpenetrating systems* and *matrix-particle systems* (see Section 2.1.1) in order to explain the different structures present in the samples. For particulate systems with monosized packings, matrix-particle structures are considered when the volume fraction of one material is less than 30%. The particles are either isolated or form small agglomerates, and can be treated as *inclusions*. Contents higher than 30 vol.% form a *percolated network of particles* that are called *interpenetrating structures*. Thus, in the samples with 90 vol.% and 80 vol.%, the nickel particles may be considered as the matrix phase and the alumina particles as inclusions. The samples 60 vol.% and 40 vol.% can be considered as interpenetrating structures. The samples with 20 vol.% and 10 vol.% alumina particles can be considered as matrix and the nickel particles as inclusions. Thereby, it is possible to expect different behaviors from these different structures as sintering proceeds.

---

[1] This part of the dissertation was partially published in:
Journal of the European Ceramic Society, v. 36, p. 2245-2253, 2016.
http://www.sciencedirect.com/science/article/pii/S0955221915303101

5.1.1 Average Contact Radius Evolution

As discussed in Section 3.2, the simulations must be stopped when the normalized average contact radius of particles attains 0.65 of the particle radius. However, due to the different sintering kinetics of nickel and alumina, the contact radius evolution of nickel-nickel, alumina-alumina and nickel-alumina contacts should be analyzed separately. All graphs concerning average contact radius (ACR) shown in this section are normalized by particle radius ($\boldsymbol{R}$) to provide generality of the simulation results. The samples are referred by their volume fraction of nickel (%).

- **Nickel-Nickel contacts**

Figure 5.1 shows the ACR evolution for nickel-nickel (Ni-Ni) contacts of the samples with nickel volume fraction of 100%, 90%, 80%, 60%, 40%, 20% and 10% over the simulation time. First of all, a quite similar behavior of all samples over the time is clearly observed. At the time *zero* (before the simulation), the ACR of all samples is about 0.003/$\boldsymbol{R}$. Then, within the first time steps of simulation, there is an abrupt increase of the ACR. After $t_s = 0.02s$, the ACR growth is smoother and with an asymptotic behavior it reaches 0.65/$\boldsymbol{R}$ at about $t_s = 0.40s$.

It is possible to observe a small difference between the curves of 100 vol.%, 90 vol.% and 80 vol.%, to the others. In these samples, alumina particles are treated as inclusions. Due to the lower sintering potential of alumina phase, its addition in metal-matrix composites tends to retard sintering and, consequently, delays Ni-Ni contact radius growth.

Other important aspect of this work is the simulation time shown in $\boldsymbol{x}$ axis. Indeed, this time is the "real time", the time that these samples would take to sinter in real life. One might say that 0.4 seconds is quite fast to sinter any sample. However, it is important to observe the sintering conditions. The particles have 100 nm of diameter. Within this size range, they have a very high surface energy and high potential to sinter [40–43]. Moreover, the samples have less than 4000 particles. It means that the total sample diameter has few μm of diameter, i.e., it is a very small sample, which would take few seconds to be sintered. In addition, it is important to observe that when the simulation starts, the

temperature is at the highest sintering temperature. There is no heating up phase for such situation. Therefore, at time zero the sintering temperature is the highest one for the process and equal to 1200 ºC. This temperature is quite high to sinter nickel, since its melting point is equal to 1455 ºC (see Table 4.4, Section 4.2), and could be expected that nickel sinters quite fast.

Figure 5.1: Average contact radius evolution (normalized by particle radius) for nickel-nickel contacts of the monosized packings over time. The samples are referred to by the volume fraction of nickel.

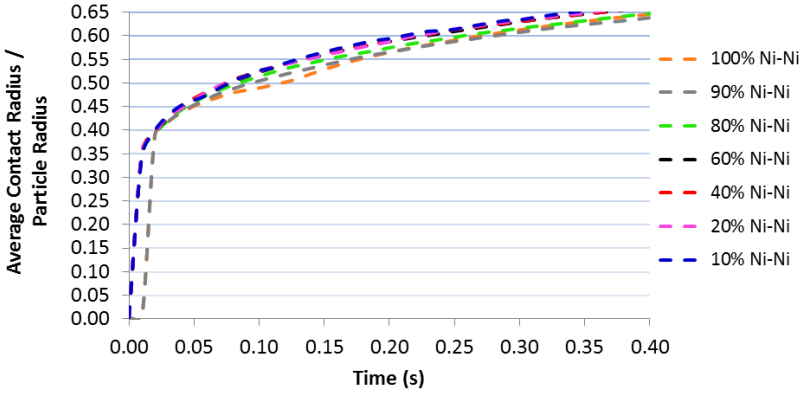

- **Alumina-Alumina contacts**

Figure 5.2 shows the ACR evolution for alumina-alumina (Al_2O_3-Al_2O_3) contacts of the samples with nickel volume fraction of 90%, 80%, 60%; 40%, 20%, 10% and 0% (pure alumina) over the simulation time. Initially, these samples have the ACR about 0.003/$\boldsymbol{R}$. Then, most of the ACR increase occurs within the earliest time steps and then it follows a smoother increase until attains about 0.3/$\boldsymbol{R}$ at $t_s = 0.40s$.

Along the simulations, the curves behavior for all samples is nearly the same and the alumina content only influences the sample 90% and 80%. In fact, the sample 90% has a more apparent increase. The high content of metal phase in this sample promotes high forces pulling the system to shrink and ends up transferring forces to sinter alumina particles.

Likely, the same behavior takes place for the sample 80%. However, the forces provided by nickel particles are more distributed through alumina ones and its effect is less pronounced. These affirmations are discussed in more detail in the next sections.

Figure 5.2: Average contact radius evolution (normalized by particle radius) for alumina-alumina contacts of the monosized packings over time. The samples are referred to by the volume fraction of nickel.

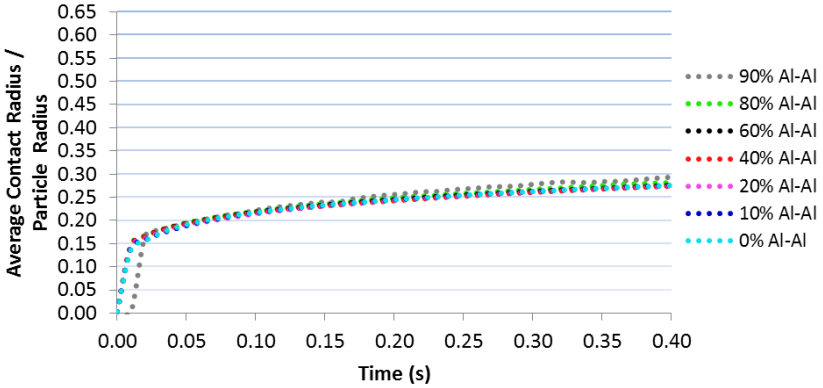

- **Comparison between Ni-Ni and Al_2O_3-Al_2O_3 contact radius evolution**

Comparing Figure 5.1 and 5.2, a noticeable difference is observed in the ACR growth between Ni-Ni and Al_2O_3-Al_2O_3 contacts. The ACR for Ni-Ni contacts is more than twice the value of Al_2O_3-Al_2O_3 contacts at $t_s = 0.40s$. As stated in Section 4.2, this behavior might be expected since nickel has a higher value of surface energy and diffusion parameter if compared to the alumina ones. These parameters lead to higher forces attracting Ni-Ni contacts and the contact radius grows faster. Therefore, an important conclusion is that ACR growth of Ni-Ni contacts is the limiting point for the simulations, since Ni-Ni contacts reach $0.65/\boldsymbol{R}$ before Al_2O_3-Al_2O_3 contacts. Consequently, the simulations are not valid after $t_s = 0.40s$ and all simulations shall be stopped at the point where Ni-Ni contacts reached value of $0.65/\boldsymbol{R}$.

Another implication of the higher ACR growth of Ni-Ni contacts is that nickel particles induce higher sintering forces through the system and faster densifications. This conclusion is discussed in

more detail in the next sections and can be confirmed by the densification curves in Section 5.1.4 further on.

Furthermore, it is possible to observe a slight variation in ACR growth of Ni-Ni and Al_2O_3-Al_2O_3 contacts only for the samples 80% and 90%. These samples are characterized as nickel-matrix composites and the alumina particles (with lower sintering potential) are considered inclusions. Then, alumina particles tend to retard the growing contact radius of Ni-Ni contacts. On the other hand, the nickel phase tends to densify the system with a high sintering force and, as consequence, to transfer forces to the alumina particles due to the particulate nature of the system.

For the samples of nickel volume fraction of 60%, 40%, 20% and 10%, the Ni-Ni and Al_2O_3-Al_2O_3 contacts are not affected by the other phase. It means that nickel and alumina phases sinter separately from each other in these samples.

- **Nickel-alumina contacts**

Figure 5.3 shows the ACR evolution for nickel-alumina (Ni-Al_2O_3) contacts of the samples with nickel volume fraction of 10% to 90% over the simulation time. Moreover, the nickel-nickel contact evolution of pure nickel sample (100%) and alumina-alumina contact of pure alumina sample (0%) are also plotted for comparison criteria.

Analyzing the Ni-Al_2O_3 contacts evolution in Figure 5.3, all samples show an ACR growth within the first time steps. From about $t_s = 0.01s$ on, the Ni-Al_2O_3 contacts start showing the ACR evolution dependent on the nickel content. For the samples 90%, 80% and 60%, the ACR growth increases as the nickel volume fraction increases. The effect of the nickel content shows stagnation for the sample 40%, 20% and 10%, whose ACR evolution follows that of the pure alumina Al_2O_3-Al_2O_3 contacts. Comparing to the pure nickel Ni-Ni contact, the Ni-Al_2O_3 contacts of all samples show slower ACR growth.

To explain the behavior of Ni-Al_2O_3 contacts, it is necessary to remember Equation 2.15 that defines the normal force acting between these contacts. As discussed in Section 2.5, there is no sintering force attracting Ni-Al_2O_3 particles. The normal force is defined only by viscous force that acts to oppose the current motion of the particles. However, the whole system is shrinking due to the sintering force acting between Ni-Ni and Al_2O_3-Al_2O_3 contacts. Then, Ni-Al_2O_3 particles tend to approximate and overlap each other as an indirect effect of the

sintering force shrinking the sample. At the same time, the viscous force between Ni-Al_2O_3 contacts acts to hinder the approximation motion of these particles.

Figure 5.3: Average contact radius evolution (normalized by particle radius) for nickel-alumina contacts of the monosized packings over time. The samples are referred to by the volume fraction of nickel. The alumina-alumina contacts from the sample 0% and nickel-nickel from sample 100% are shown as reference.

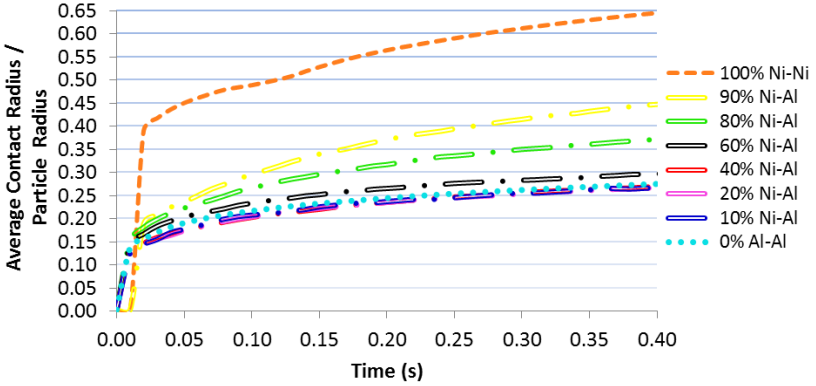

Furthermore, it was stated previously that nickel particles induce higher sintering forces to the system due to the faster ACR growth than alumina. From this conclusion, one may consider that there is a higher total force pulling the system to shrink when a higher content of nickel is present in the sample. Thus, higher nickel volume fraction results in higher total force shrinking the system and the effect of the viscous force between Ni-Al_2O_3 contacts are less pronounced. In other words, the effect of the viscous force between Ni-Al_2O_3 contacts is reduced as the nickel content increases. This occurs due to the higher total forces promoted by higher nickel contents in order to shrink to system.

This explanation can be easily understood mainly for the samples 90 vol.% and 80 vol.%. In these samples, the alumina particles are essentially isolated particles and surrounded by nickel particles. Thus, the Ni-Al_2O_3 contacts suffer higher influences from the nickel behavior (higher densifications). For the samples 40 vol.%, 20 vol.% and 10 vol.%, the higher alumina content promotes weaker sintering forces through the system and the Ni-Al_2O_3 contacts essentially follow

the ACR growth of the Al_2O_3-Al_2O_3 contacts. Even though the sample 60 vol.% is considered as an interpenetrating structure, the higher nickel content influences slightly the Ni-Al_2O_3 contacts and its ACR growth is a bit higher than the samples 40 vol.%, 20 vol.% and 10 vol.%.

Once again, it is important to remember that this explanation above is supported by the densification curves further on.

5.1.2 Average Coordination Number Evolution

Coordination number (CN) of each particle is defined as the number of neighboring particles in contact. As sintering proceeds, due to the shrinkage of the system and the rearrangement of the particles, CN tends to increase along the process. For a mixture of two materials, CN is an important parameter, which is related to the homogeneity of the particle distribution. Thus, CN of the three kinds of contact shall be analyzed separately since their evolution along sintering is not the same.

It is important to point out that the average CN presented in this work shows slightly smaller values if compared to those presented in some works in literature [20, 22]. This is because no periodic boundary conditions were implemented for the numerical samples. Thereby, the particles on the packing border have lower CN and this reduces the average. Furthermore, in order to confirm that the lack of boundary conditions is not affecting the results, few simulations with a larger number of particles have been carried out and are presented in a section forward.

- **Nickel particles with nickel contacts**

Figure 5.4 shows the average coordination number (ACN) evolution for nickel particles with nickel contacts (Ni→Ni) of the samples with nickel volume fraction of 100%, 90%, 80%, 60%, 40%, 20% and 10% over the simulation time. Before the simulations, ACN of all samples is smaller than 3.5 and it decreases as the nickel content decreases. Once the sintering has started, ACN increases along the simulation, as expected. Overall, ACN growth is higher as the nickel content increases.

Figure 5.4: Average coordination number evolution for nickel particles with nickel contacts of the monosized packings over time. The samples are referred to by the volume fraction of nickel.

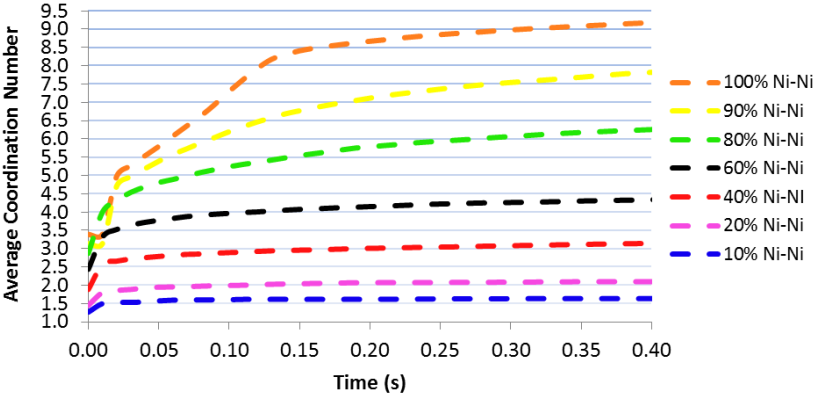

For the samples 20 vol.% and 10 vol.%, there is a small ACN growth within $t_s = 0.02s$ and then the curves are virtually constant until the end of the simulation. Within the first time steps, every Ni-Ni contact close to each other is formed and this configuration continues due the low nickel content.

For the samples 40 vol.% and 60 vol.%, there is a sudden ACN growth within $t_s = 0.02s$ and then the curves grow slightly until the end of the simulation. This behavior is due to the interpenetrating structures. Even though the nickel particles have a limited number of nickel neighbors in such structures, the continuous network of particles allows the development of new Ni-Ni throughout the whole process.

For the samples 80 vol.%, 90 vol.% and 100 vol.%, an abrupt ACN growth takes place within $t_s = 0.02s$. Thereafter, it continues clearly increasing as the simulation proceeds. This increase is higher as the nickel content increases. Such a behavior is rather different if compared to the sample with nickel content lower than 80 vol.%. As nickel particles are considered the matrix for these systems, many new Ni-Ni contacts are developed along the whole sintering process.

- **Alumina particles with alumina contacts**

Figure 5.5 shows the ACN evolution for alumina particles with alumina contacts of the samples with nickel volume fraction of 90%, 80%, 60%, 40%, 20%, 10% and 0% over the simulation time. Initially,

the sample 0 vol.% has ACN of 3.4 and the value decreases as the alumina content decreases. As the simulation proceeds, ACN of all samples naturally increases. This increase is higher as the alumina content increases.

For the sample 90 vol.% and 80 vol.%, the alumina particles are essentially isolated and have a limited number of neighboring alumina particles to develop new Al_2O_3-Al_2O_3 contacts. ACN increase for these samples is very small during the whole process.

For the samples 60 vol.% and 40 vol.%, ACN increase of Al_2O_3-Al_2O_3 is more noticeable due to the continuous network of alumina particles.

Figure 5.5: Average coordination number of alumina particles with alumina contacts of the monosized packings over time. The samples are referred to by the volume fraction of nickel.

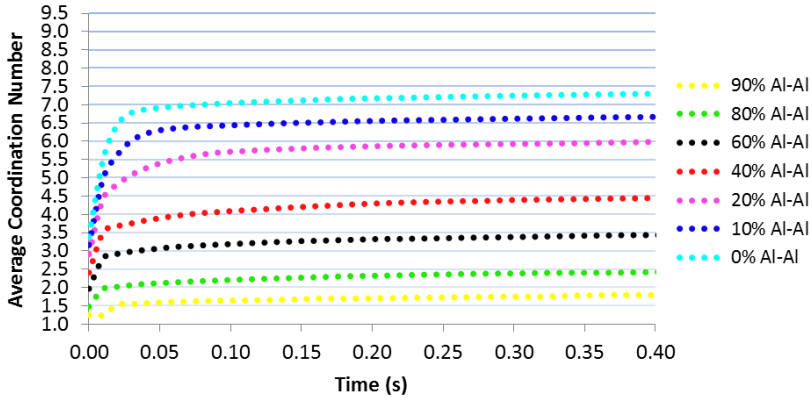

For the samples 20 vol.%, 10 vol.% and 0 vol.%, the alumina particles represent the matrix phase, which have many neighboring alumina particles to develop new Al_2O_3-Al_2O_3 contact through the whole simulation. Nevertheless, most of the ACN increase occurs within about $t_s = 0.05s$. After that, the ACN increase is very slight.

- **Comparison between Ni-Ni and Al_2O_3-Al_2O_3 coordination number evolution**

Comparing Figures 5.4 and 5.5, it is possible to realize some similarities and some differences. In general, the increase of ACN for all

sample of both Ni-Ni and Al_2O_3-Al_2O_3 have the highest increase within the earliest simulation time. This is because there are higher forces pulling the system to shrink in the beginning of the process. Thus, most of the possible contacts are developed with neighboring particles in the beginning.

First of all, a comparison is made for ACN evolution of isolated particles (Al_2O_3-Al_2O_3 of 90 vol.% and Ni-Ni of 10 vol.%; Al_2O_3-Al_2O_3 of 80 vol.% and Ni-Ni of 20 vol.%). For both pair of samples, the behavior is practically the same. It means that these four samples can really represent matrix-particle systems.

For the interpenetrating systems, ACN growth is also essentially the same, when comparing Ni-Ni contacts of the sample 60 vol.% with Al_2O_3-Al_2O_3 contacts of the sample 40 vol.% and Ni-Ni contacts of the sample 40 vol.% with Al_2O_3-Al_2O_3 contacts of the sample 60 vol.%.

On the other hand, visible distinction may be observed when the ACN evolution of the matrix phase is compared. The ACN growth of Ni-Ni contacts when nickel is the matrix phase (samples 100 vol.%, 90 vol.% and 80 vol.%) is higher than Al_2O_3-Al_2O_3 contacts when alumina is the matrix (samples 0 vol.%, 10 vol.% and 20 vol.%). It means that more Ni-Ni contacts are developed along the process when nickel is the matrix if compared to the Al_2O_3-Al_2O_3 contacts when alumina is the matrix. This is another effect and confirmation that nickel particles promote higher sintering forces and faster shrinkage of system.

- **Nickel particles with alumina contacts**

Figure 5.6 shows the ACN evolution of nickel particles with alumina contacts (Ni→Al_2O_3) for the samples with nickel volume fraction of 90%, 80%, 60%, 40%, 20% and 10% over the simulation time. The ACN evolution of Ni-Ni contacts for pure nickel sample (100%) and Al_2O_3-Al_2O_3 contact for pure alumina sample (0%) are also plotted by comparison issue. Note that it is being analyzed in Figure 5.6 the average number of alumina particles contacting each nickel particles. It is not the same than ACN of alumina particles with nickel contacts. The results would be completely different. For this reason, this parameter is referred as Ni→Al.

Considering Ni→Al_2O_3 contacts, ACN increases as the alumina content increases. It means that there are more alumina particles surrounding (and contacting) the nickel particles when higher alumina content is present in the sample. ACN increase for all samples is quite

smaller than for both Ni-Ni contacts of pure nickel sample and for Al_2O_3-Al_2O_3 contacts of pure alumina sample.

Figure 5.6: Average coordination number evolution for nickel particles with alumina contacts of the monosized packings over time. The samples are referred to by the volume fraction of nickel. The alumina-alumina CN from the sample 0% and nickel-nickel CN from sample 100% are shown as reference.

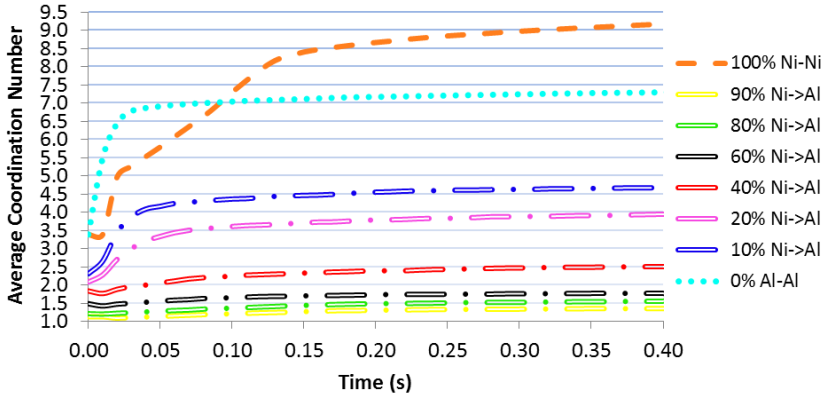

For the samples 10 vol.% and 20 vol.%, ACN increase is more noticeable within about $t_s = 0.15s$ and then its increase is smoother. As in these samples the nickel particles are mostly surrounded by alumina particles, several contacts may be developed by nickel particles with alumina.

For the samples 90 vol.% and 80 vol.%, ACN increase is very slight during the whole simulation and can be considered constant for such a case. The few alumina contacts of the nickel particles are already formed in the beginning of the process and the low alumina content does not allow new Ni→Al_2O_3 contacts to be developed.

Even though the number of interfaces between nickel and alumina should be higher for the samples 60 vol.% and 40 vol.%, ACN increase of Ni→Al_2O_3 does not follow a behavior that one might expect. This occurs due to the interpenetrating structures of the phases and its effect during sintering. The nickel and alumina phase densify independently from each other for the samples 60 vol.% and 40 vol.%. It means that nickel particles tend to approach other nickel particles and the same happens with alumina. This situation is more pronounced for the sample 60 vol.% where only few new Ni→Al_2O_3 contacts are

developed. Due to the higher alumina content in sample 40 vol.%, more Ni→Al_2O_3 contacts are developed during the simulation, although the behavior described before is also present.

5.1.3 Visual Analysis of the Monosized Samples

In order to visualize the different sintering behaviors discussed in Sections 5.1.1 and 5.1.2, Figure 5.7 shows screenshots of the sample 80 vol.% (matrix-particles structures) and 60 vol.% (interpenetrating structures). Figure 5.7 (a) shows the sample 80 vol.% before the simulation and (b) after the simulation. Figure 5.7 (c) shows the sample 60 vol.% before the simulation and (d) after the simulation. In these screenshots, a cross section of the samples is shown at the middle of axis $\boldsymbol{x}$ (see the coordinate axes) to visualize inside the packing. The gray particles represent nickel, whereas blue particles represent alumina. Note that the green lines represent the initial size of the spherical simulation box.

In Figures 5.7 (a) and (b), it is possible to observe that the whole sample of 80 vol.% shrinks along the simulation. The edges of the sample move away considerably from the initial simulation box size. Indeed, this is a qualitative (visual) confirmation that this sample is densifying. Furthermore, as nickel is the matrix phase for such a case, the nickel phase probably controls the densification throughout the sintering process.

On the other hand, the sintering behavior of the sample 60 vol.% in Figure 5.7 (c) and (d) is rather distinct. The final distance of the sample borders to the initial simulation box size is less pronounced than in the sample 80 vol.%. It is observed that nickel particles are highly densified with large contact radius developed between Ni-Ni contacts through the continuous network of particles. Meanwhile, the alumina particles are barely densified and the Al_2O_3-Al_2O_3 contact radius is quite small. This is in agreement with the average contact radius evolution for Ni-Ni and Al_2O_3-Al_2O_3 contacts shown in Section 5.1.1.

Figure 5.7: Screenshots of the numerical samples during sintering: (a and b) initial and final configuration of the sample 80 vol.% of nickel; (c and d) initial and final configuration of the sample 60 vol.% of nickel.

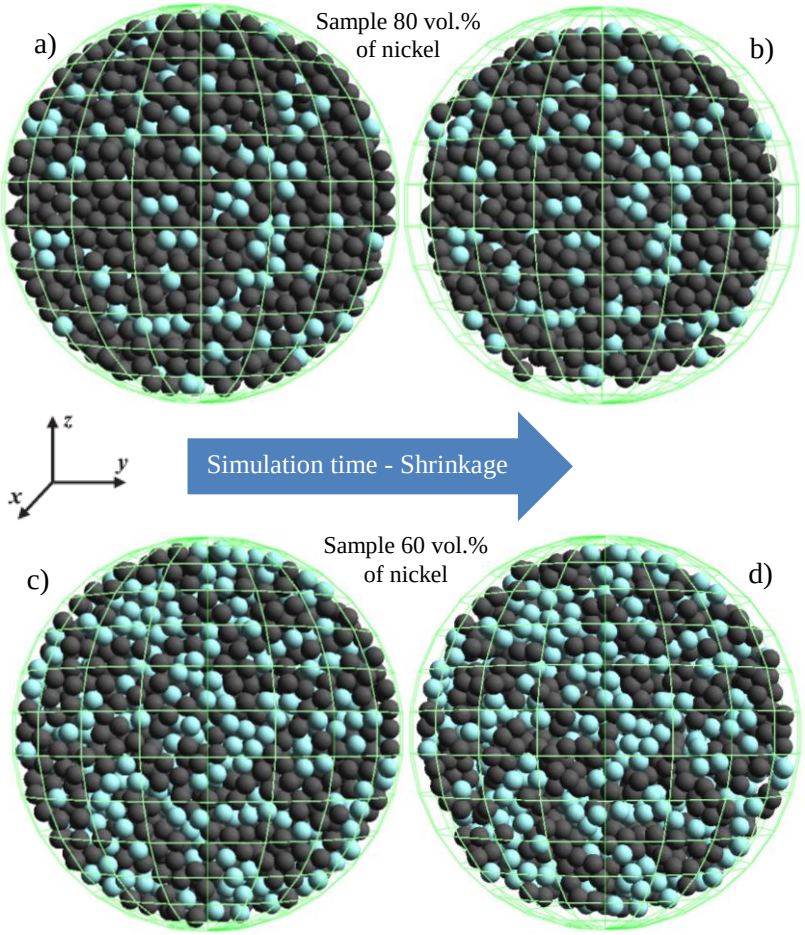

Still in Figure 5.7 (d), several empty spaces can be seen among nickel-alumina interfaces due to the high attraction between Ni-Ni particles. This supports the low increase of the ACN for Ni→Al_2O_3 shown in Figure 5.6 for the sample 60 vol.%. Moreover, grain growth should occur among nickel particles from that point of the simulation on

($t_s = 0.40s$) to simulate the process realistically, as discussed previously.

These qualitative statements about Figure 5.7 are supported quantitatively by the densification curves in the next section.

5.1.4 Global Densification

Figure 5.8 shows the global relative density (RD) evolution of the monosized samples with nickel volume fraction of 100%, 90%, 80%, 60%, 40%, 20%, 10% and 0% over the simulation time. It is observed that RD increases for all samples along the process. However, RD increase for the samples with nickel volume fraction lower than 80% is very small and completely different whether compared to the samples 100 vol.%, 90 vol.% and 80 vol.%.

Figure 5.8: Global relative density evolution of all monosized samples over time. The samples are referred to by the volume fraction of nickel.

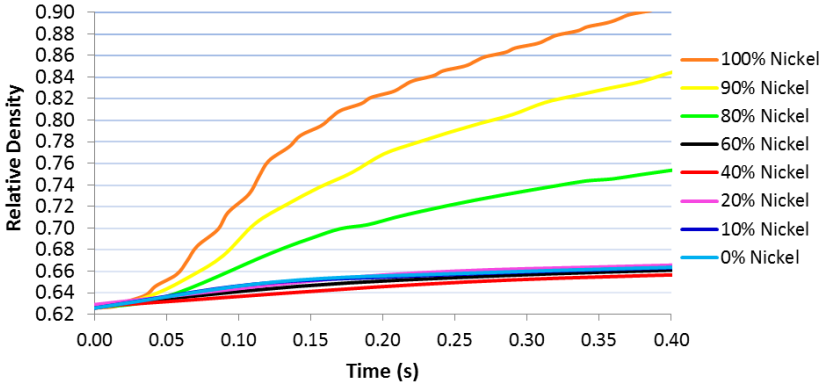

Observing Figure 5.8, the relative density evolution of the whole sample is highly dependent of sample composition. The sample with pure nickel (100 vol.%) shows the highest RD increase among all samples. As there are no alumina particles to retard the densification, the sample follows the nickel sintering kinetics.

Comparing the samples of pure nickel (100 vol.%) and pure alumina (0 vol.%), the nickel shows a faster densification evolution than alumina. It confirms that the nickel parameters lead to higher total forces to shrink and densify the system during sintering.

Comparing the samples 90 vol.% and 80 vol.% with the sample 100 vol.% (nickel-matrix composite), the RD growth is reduced as the alumina content increases. As discussed previously (see Section 2.5), nickel and alumina contacts are not sintering and solely viscous forces describe their contacts. Thereby, alumina particles offer a resistance for the shrinkage of the system and this resistance is higher as the alumina content increases. Moreover, it should be recalled that the samples 90 vol.% and 80 vol.% represent matrix-particle system, where nickel is the matrix phase. For this reason, the nickel particles are able to drive the shrinkage of the whole system and proceed with the densification.

For the samples 60 vol.%, 40 vol.%, 20 vol.%, 10 vol.% and 0 vol.%, RD evolution is very slight and virtually the same. RD of these samples increases only from 0.62 to about 0.66 at $t_s = 0.4s$. The densification of these samples is essentially controlled by the alumina kinetics.

This statement can be more easily understood for the samples 10 vol.% and 20 vol.%. These two samples are considered matrix-particle system, where alumina phase is the matrix. Thus, the alumina phase drives the shrinkage of the packing. The resistance imposed by the nickel particles is very slight and can be neglected for such a case.

As discussed in the last sections, the nickel and alumina phase sinter separately from each other through the interpenetrating structures (samples 60 vol.% and 40 vol.%). Furthermore, it was shown that the average contact radius growth (see Section 5.1.1) of nickel is rather faster than the alumina one, resulting in different densification kinetics. Thus, while the continuous network of nickel particles is in advanced stage of the sintering, the alumina one is many steps back. Thereby, globally the samples 60 vol.% and 40 vol.% shall present the densification of the system basically controlled by the slowest kinetic step. In this case, this is the alumina phase.

The findings described in this section are in line with those presented in the sections about average contact radius evolution, average coordination number evolution and qualitative analysis of the sample (Sections 5.1.1, 5.1.2 and 5.1.3, respectively).

5.1.5 Samples with Higher Number of Monosized Particles

Simulations of monosized samples with larger number of particles have been carried out in order to proof that the lack of periodic boundary conditions is not affecting the simulation results and the main

conclusions. The nickel volume fraction is the same of the smaller samples (pure nickel, nickel volume of 90, 80, 60, 40, 20 and 10% and pure alumina) but the number of particles is four times higher (~16,000 particles in each sample).

Figure 5.9 shows global relative density evolution of all larger monosized samples over the simulation time. Note that the simulation time is longer than for the smaller samples. Thus, it is possible to conclude that the trends are valid even for longer simulation times.

Figure 5.9: Global relative density evolution of all monosized samples with 16,000 particles over time. The samples are referred to by the nickel volume fraction.

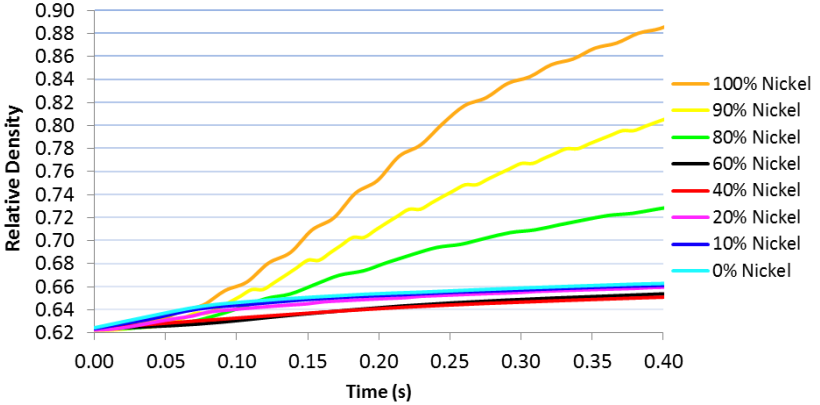

Comparing Figures 5.9 and 5.8 (RD evolution of the larger and smaller samples, respectively), it is confirmed that the boundary conditions do not affect the overall results. The trend of the curves are essentially the same, in which pure nickel shows the highest RD evolution, followed by the sample of 90 and 80 vol.%. In addition, one may realize the retarded densification of samples 60 and 40 vol.%, which is slightly more pronounced here.

5.1.6 Discussion of Monosized Packings

The monosized packing results presented along this chapter can be divided into two categories. Firstly, some general trends are discussed. The highest growth of the average contact radius and the coordination number occurred within the beginning of the simulation, regardless the type of contact (Ni-Ni, Al_2O_3- Al_2O_3 or Ni-Al_2O_3). Such a

behavior is explained by the high potential of the particles to sinter at the initial step, when no viscous forces exist to provide a resistance for sintering. This was explained in Section 3.4 (Figures 3.6 and 3.7), in which high forces were observed pulling the particles together and resulting in high velocities. Therefore, simulations of metal-ceramic composites are also following this expected behavior of samples with one phase.

Due to the substantial difference between sintering potential of nickel and alumina material, it was needed to outline which phase would define the stopping point for the simulation. Nickel particles have higher surface energy and diffusion parameter and sinters quite faster than alumina particles. Ceramic particles barely densified as metal particles already reached the final relative density of 90% (represented by the contact radius of 65% of the particles radius). This is clearly observed in ACR charts (Figure 5.1 and 5.2). Thus, nickel particles define when the simulation must be stopped.

Beyond these general behaviors found for all samples, there are some related to the content of metal and ceramic phase. From this point of view, the results can be divided into three groups: metal-matrix composite, ceramic-matrix composite and interpenetrating structure.

For the nickel-matrix composites (samples 80%, 90% and 100% volume of nickel), the sintering is driven by the nickel kinetics. It is important to remember that in matrix-particulate composite materials within this range of content, ceramic phase is added as hard inclusions and has the purpose to reinforce the composite [7]. Typically, ceramic phase (such as alumina) has lower sintering activity than the metal one and, thereby, its addition into metal-matrix sample as inclusions retards densification [5]. From this knowledge, the densification curve (Figure 5.8) shows the pure metal sample with the highest densification rate and it decreases as the alumina content is increased.

Additionally, the sample of 90 vol.% shall be analyzed individually. In this volume content (10%) the alumina particles are essentially isolated particles. This content is enough to reduce the densification, even though the final relative density is comparable to the pure metal sample. These findings are in line with the simulation results of Martin et al. [20] and experimentally derived results of Olmos et al. [5] as well as of Nakada and Kimura [44]. Those authors claim that rigid particles in a matrix retard the sintering leading to longer sintering time but still comparable relative densities.

When the ceramic content is increased to 20%, the alumina phase is not isolated as inclusions anymore. Here, they form small aggregates and agglomerates (see Figure 5.7 a). As shown in Figure 5.4, the coordination of Ni-Ni is reduced and, consequently, the sintering potential is restrained as well. Once again, this result is in agreement with Yan et al.'s work [6], in which the authors varied the content of inclusions.

Nevertheless, the alumina agglomerates in the sample 80% are sintering as well. Analyzing the evolution of ACR for the Ni-Al_2O_3 contact (Figure 5.3), one can recognize a relatively high value for nickel–matrix composites. This evolution of ACR between nickel and alumina particles is promoted by forces acting on these contacts. As the nickel particles drive the system and promote densification, they develop new contacts with other nickel particles as well as with alumina particles. Because of the particulate structure of the system, the sintering forces are distributed to all contacting particles.

The second group of results is the alumina-matrix composites, which considered samples with nickel volume of 10%, 20% and pure alumina (sample 0%). As exposed previously, alumina has a lower sintering activity than nickel and the global densification of them is very small (only ~4%). Indeed, sintering of alumina particles occurs only slightly. One might say that the sample is just creating necks but not densifying. This observation is in agreement with experimental observations of sintering of submicron alumina particles at 1200 ºC [45]. At the temperature used in the simulation (1200 ºC), it would be necessary much longer simulation time to reach comparable relative densities for such samples. One possible suggestion would be to increase the time step. However, this alternative is not valid here because the nickel parameters defined the maximum time step for the simulation and its increase would lead to numerical instability.

The last group is the interpenetrating structure (samples nickel fraction 40 and 60 vol.%). The global densification of them is very small and basically follows the alumina kinetics. Looking at Figures 5.7 c) and d), it can be observed that the nickel and alumina phases form a continuous network of particles. The densification of each phase occurs separately. As the metal particles already reached the densification of 90%, alumina particles are only at 66%. Since there are many contacts between metal and ceramic phase, several defects (cracks) are developed through the sample and the initial configuration is destroyed.

5.2 BIMODAL PACKINGS

In this section, the results concerning the simulations of the packings with varying nickel particle size are presented and discussed. The first part shows the average contact radius evolution for nickel-nickel, alumina-alumina and nickel-alumina contacts. Then, the coordination number evolution is presented for the three kinds of contacts as well. Finally, the global relative density evolution for all bimodal samples is presented and compared. Beyond the bimodal packings, the monosized packing with nickel volume fraction of 60% (the same content than the bimodal packings) is also presented along this section for comparison criteria. This sample is referred to as particle size ratio 1.0.

It is important to recall that the nickel volume fraction is equal to 60% for all samples, which means that they are interpenetrating structures. Furthermore, the simulation box size has been kept constant and it leads to the reduction of the number of nickel particles as the nickel particle size increase (see Table 4.2 in Section 4.1).

5.2.1 Average Contact Radius Evolution

The average contact radius (ACR) is the limiting point for the simulation of bimodal packing as well as it was for the monosized packing. The three kinds of contacts (nickel-nickel, alumina-alumina and nickel-alumina) are analyzed separately due to their different evolution. Their respective particles radius $\boldsymbol{R}$ normalizes the ACR of each sample. The bimodal samples are referred to by the ratio of their nickel particle radius to the alumina particles radius.

- **Nickel-nickel contacts**

Figure 5.10 shows ACR evolution for nickel-nickel (Ni-Ni) contacts of the samples with particle radius ratio of 1.0, 1.5, 2.0, 2.5 and 3.0 over the simulation time. First, a noticeable influence of the particle radius is observed on the ACR growth. Note that the simulation time in this Figure is rather longer ($t_s = 5.0s$) if compared to that one used to simulate the monosized packings ($t_s = 0.40s$).

Analyzing Figure 5.10, ACR growth of Ni-Ni contacts is clearly slower as the particle size increases. This behavior is quite well theoretically established since smaller particles have higher total surface

energy and induce higher driven force for sintering (see Section 2.3.1.2). Moreover, such a behavior can be also understood by the normal force acting between Ni-Ni contacts (Equation 2.11 in Section 2.5). The sintering term in this equation increases linearly as the particle radius increases. On the other hand, the viscous term increases as the contact radius increases in the fourth power. As larger particles develop larger contact radius, the viscous term (resistance) opposing the approximation motion of these particles is higher. Therefore, the normal force acting to attract a pair of particles is smaller for larger particles.

Figure 5.10: Average contact radius evolution (normalized by particle radius) for nickel-nickel contacts of the bimodal packings over time. The samples are referred to by the nickel-alumina particle size ratio.

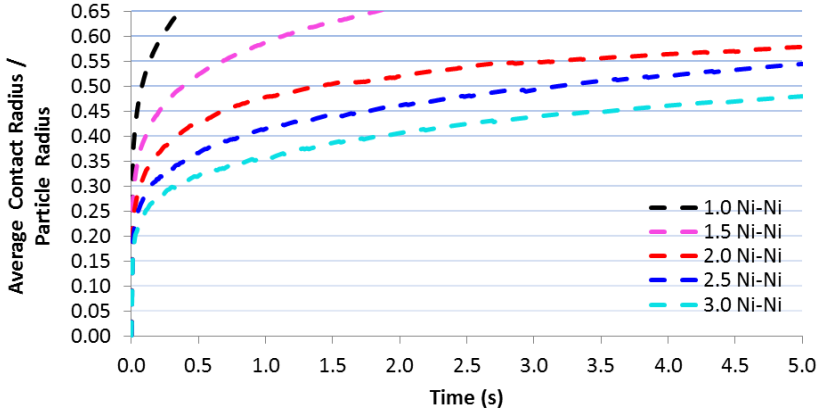

As consequence of these different kinetics caused by the particles radius, the simulation time to attain the limiting point (0.65/***R***) increases as the particles radius increases. While sample 1.0 (monosized packing 60 vol.%) reaches the limiting point at $t_s = 0.4s$, the bimodal sample 1.5 does at about $t_s = 1.8s$. The samples 2.0, 2.5 and 3.0 do not reach the limit contact radius within the simulation time carried out of $t_s = 5.0s$. The final ACR reached by these samples is higher as the particle radius ratio decreases. It should be pointed out that the increase in time is not linear due to the relation in the fourth power of the contact radius, as stated previously.

- **Alumina-alumina contacts**

Figure 5.11 shows the ACR evolution for alumina-alumina contacts (Al_2O_3-Al_2O_3) of the samples with particle radius ratio of 1.0, 1.5, 2.0, 2.5 and 3.0 over the simulation time.

Figure 5.11: Average contact radius evolution (normalized by particle radius) for alumina-alumina contacts of the bimodal packings over time. The samples are referred to by the nickel-alumina particle size ratio.

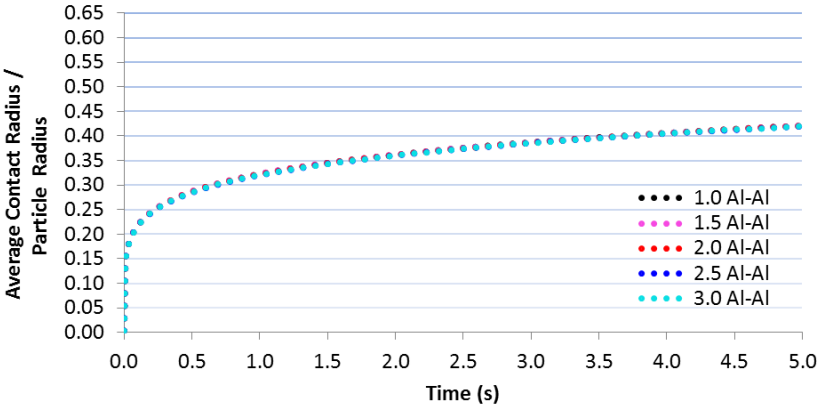

No difference is observed in Figure 5.11 in ACR growth of Al_2O_3-Al_2O_3 contacts for these samples, as expected. Since the alumina particles have the same size in all samples, the growth kinetic of ACR is the same. Furthermore, as the number and size of alumina particles are the same in the monosized and bimodal samples, these curves are in accordance with those obtained by the ACR growth of Al_2O_3-Al_2O_3 contact for the monosized packing (Figure 5.2 in Section 5.1.1).

- **Comparison between Ni-Ni and Al_2O_3-Al_2O_3 contact radius evolution**

In order to compare the ACR growth of Ni-Ni and Al_2O_3-Al_2O_3 contacts, Figure 5.12 shows the curves of both contacts. Only one curve of Al_2O_3-Al_2O_3 contacts is plotted (sample 3.0) since these contacts are essentially the same for all samples (see Figure 5.10).

Figure 5.12: Comparison of the average contact radius evolution (normalized by particle radius) of Ni-Ni and Al_2O_3-Al_2O_3 contacts of the bimodal packings over time. The samples are referred to by the nickel-alumina particle size ratio.

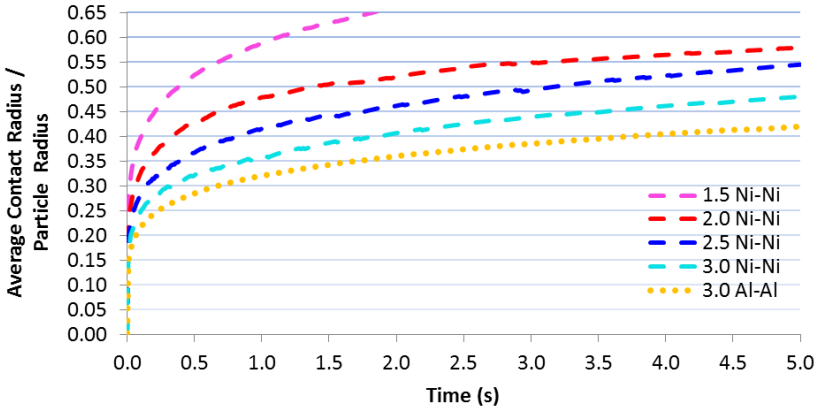

Analyzing Figure 5.12, ACR growth of Ni-Ni contacts reduces and tends to approximate to the Al_2O_3-Al_2O_3 contacts curve as the nickel particles size increases. However, the ACR growth of the largest nickel particle (sample 3.0) is faster than the alumina one. Nevertheless, one may expect that for a certain nickel particle size, the ACR growth of Ni-Ni contacts would became slower than alumina. This proposition could be tested for further works with the particles size ratio at most 4.0 times larger. This is because the generalization used in this work (see Equation 2.16 in Section 2.5) for bimodal pair of particles is valid up to this limit.

Therefore, it is concluded that nickel has the fastest sintering kinetic and determines the limiting point of the simulations for the size ratio used in this work.

- **Nickel-alumina contacts**

Figure 5.13 shows the ACR evolution for nickel-alumina (Ni-Al_2O_3) contacts of the samples with particle size ratio of 1.0, 1.5, 2.0, 2.5 and 3.0 over the simulation time. The Al_2O_3-Al_2O_3 evolution of the sample 3.0 is also plotted by comparison criteria.

Observing the ACR growth of Ni-Al_2O_3 contacts, one might realize a certain tendency. Considering the sample 1.0, 1.5 and 2.0, the increase of ACR is slower as the nickel particle size increases. The

evolution for the samples 2.0, 2.5 and 3.0 are quite similar and can be neglected for such a small variation.

Figure 5.13: Average contact radius evolution (normalized by particle radius) for nickel-alumina contacts of the bimodal packing over time. The samples are referred to by the nickel-alumina particle size ratio.

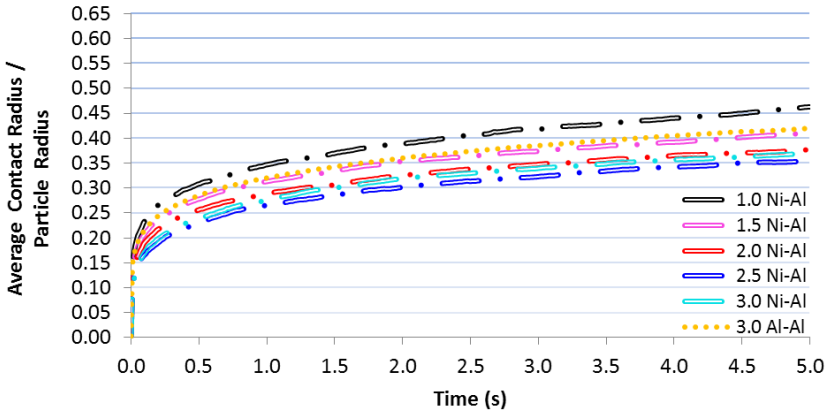

The behavior of the samples 1.0, 1.5 and 2.0 can be an effect of the weaker forces promoted by larger nickel particles, which was discussed previously in this section. Thus, the total force shrinking the system is smaller when larger particles are present and the effect of the viscous forces acting between Ni-Al_2O_3 (see Equation 2.13 in Section 2.5) is more pronounced.

When compared to the Al_2O_3-Al_2O_3 contact radius evolution, Ni-Al_2O_3 contacts with particle size ratios larger than 2.0 show slower ACR growth. It means that the global influence caused by larger nickel particles is less pronounced.

5.2.2 Average Coordination Number Evolution

The coordination number may show a substantial variation due to the particle size increase. Thus, the average coordination number (ACN) of the bimodal samples is analyzed separately for each kind of contact: nickel particles with nickel contacts, alumina particles with alumina contacts and nickel particles with alumina contacts.

- **Nickel particles with nickel contacts**

Figure 5.14 shows the ACN evolution for nickel particles with nickel contacts (Ni→Ni) of the samples with particle size ratios of 1.0, 1.5, 2.0, 2.5 and 3.0 over the simulation time. Note that the highest value of the ACN is 5. As expected, ACN increases for all samples and it occurs within the earliest simulation times.

Figure 5.14: Average coordination number evolution for nickel particles with nickel contacts of the bimodal packing over time. The samples are referred to by the nickel-alumina particle size ratio.

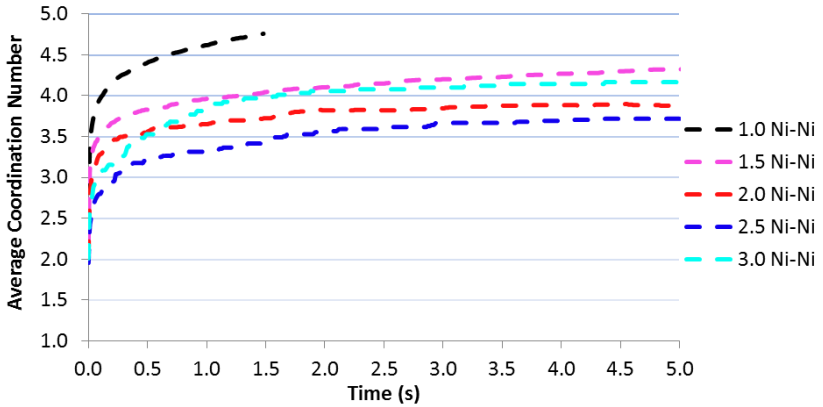

Comparing the samples 1.0, 1.5, 2.0 and 2.5, it is possible to observe a tendency. The increase of ACN is smaller as the particles size increases. The reason for such a behavior is the reduction of the total number of nickel particles as the particle size increases (see Table 4.2 in Section 4.1). As discussed previously, in order to keep the simulation box size constant and at the same time increase the nickel particle size (for the same volume fraction), it is necessary to reduce to number of nickel particles. Thus, larger nickel particles have less nickel neighbors to develop contacts and the ACN decreases.

However, the sample 3.0 does not follow the behavior previously described in Figure 5.14. This sample shows an increase of ACN higher than the sample 2.0 and 2.5, and close to the sample 1.5. Likely, this is because the nickel particles are not so homogeneously distributed through the sample 3.0, as it can be seen in the cross-section of this sample in Figure 5.14. This sample has only 92 nickel particles. For such a small number of particles, any small heterogeneity

(unavoidable in random packing of particles) might cause these differences in the coordination number.

Figure 5.15: Cross-section of the sample 3.0.

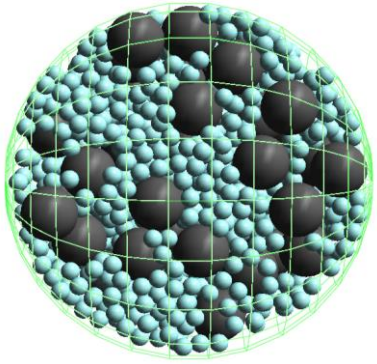

- **Alumina particles with alumina contacts**

Figure 5.16 shows the ACN evolution for alumina particles with alumina contacts of the samples with particle size ratio of 1.0, 1.5, 2.0, 2.5 and 3.0 over the simulation time. Once again, the highest value of the ACN is 5.

In Figure 5.16, ACN increases for all samples as simulation proceeds and it occurs within the earliest simulation times. This increase is higher as the nickel particle size increases, though the differences are very slight. The reason for this behavior is related to the spatial distribution of nickel and alumina volumes through the bimodal samples. As already reported, the nickel particles size has been increased to the same volume fraction. Hence, the same nickel volume that was widely spread through the monosized sample is in turn clustered in the larger particles. In other words, the nickel volume spatial distribution decreases as the particle size increases. Meanwhile, alumina particles are also more clustered as the nickel particle size increases and have more neighboring alumina to develop more Al_2O_3-Al_2O_3 contacts. This explanation is supported by the samples screenshots in the next section.

Figure 5.16: Average coordination number evolution for alumina particles with alumina contacts of the bimodal packing over time. The samples are referred to by the nickel-alumina particle size ratio.

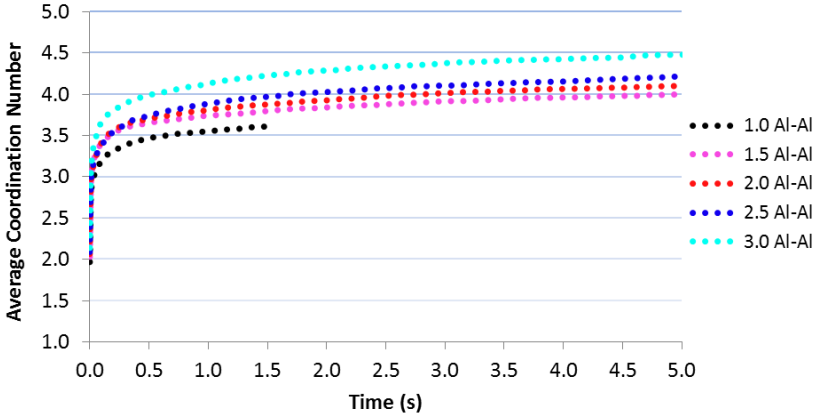

- **Nickel particles with alumina contacts**

Figure 5.17 shows the ACN evolution for nickel particles with alumina contacts (Ni→Al) of the samples with particle size ratios of 1.0, 1.5, 2.0, 2.5 and 3.0 over the simulation time. In this case, the highest value on the ACN is 15.

Looking at Figure 5.17, large differences can be observed for the ACN evolution of Ni→Al_2O_3 along the simulations. The increase of ACN is higher as the nickel particle size increases. Indeed, the distance between pairs of close curves is higher as the particle size increases. The explanation for such a behavior is due to the ratio between the particles size. Larger nickel particles have larger surface area. It means that they have superficial space to develop larger number of contacts for a given size of alumina particles. This behavior is rather evident and it should be expected. Nevertheless, it is important to note that it is shown the average of the coordination number. If the total number of Ni→Al_2O_3 contacts was presented instead the average, it would be smaller the larger nickel particles.

In fact, this behavior related to the ACN of Ni→Al_2O_3 is very important to the overall sintering behavior. It may explain an unexpected behavior found in the global densification, which is explored in the next sections.

Figure 5.17: Average coordination number evolution for nickel particles with alumina contacts of the bimodal packing over time. The samples are referred to by the nickel-alumina particle size ratio.

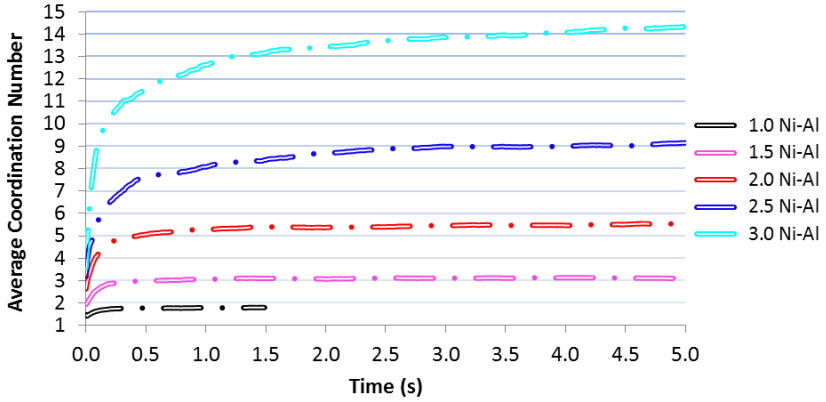

5.2.3 Visual Analysis of the Bimodal Packings

Figure 5.18 shows screenshots of the bimodal samples before and after the simulation in order to analyze the samples qualitatively. The smallest and the largest particles size ratio are shown. Figure 5.18 (a) shows the sample of ratio 1.5 before the simulation and (b) after the simulation ($t_s = 2.0s$). Figure 5.18 (c) shows the sample of ratio 3.0 before the simulation and (d) after the simulation ($t_s = 5.0s$). These differences in the final simulation time are due to the difference contact radius growth in these samples (see Figure 5.10 in Section 5.2.1). The screenshots show a cross section of the samples at the middle of axis $\boldsymbol{x}$ (see the coordinate axes) to visualize inside the packing. The gray particles represent nickel whereas blue particles represent alumina particles. Note that the green lines represent the initial size of the spherical simulation box.

In Figure 5.18 (a) it is observed that the sample of ratio 1.5 has nickel and alumina particles well distributed all over the packing. Comparing to the sample of ratio 1.0 (monosized samples 60 vol.% in Figure 5.7 (c) in Section 5.1.3), it is possible to notice the spatial distribution of volume changes in ratio 1.5 due to the larger nickel particles, as discussed in the last section. In Figure 5.17 (b), the edges of the sample move away slightly from the initial simulation box size. Hence, small densification should be expected.

Figure 5.18: Screenshots of the bimodal samples during sintering: (a and b) initial and final configuration of the sample with particle size ratio 1.5; (c and d) initial and final configuration of the sample with particle size ratio 3.0.

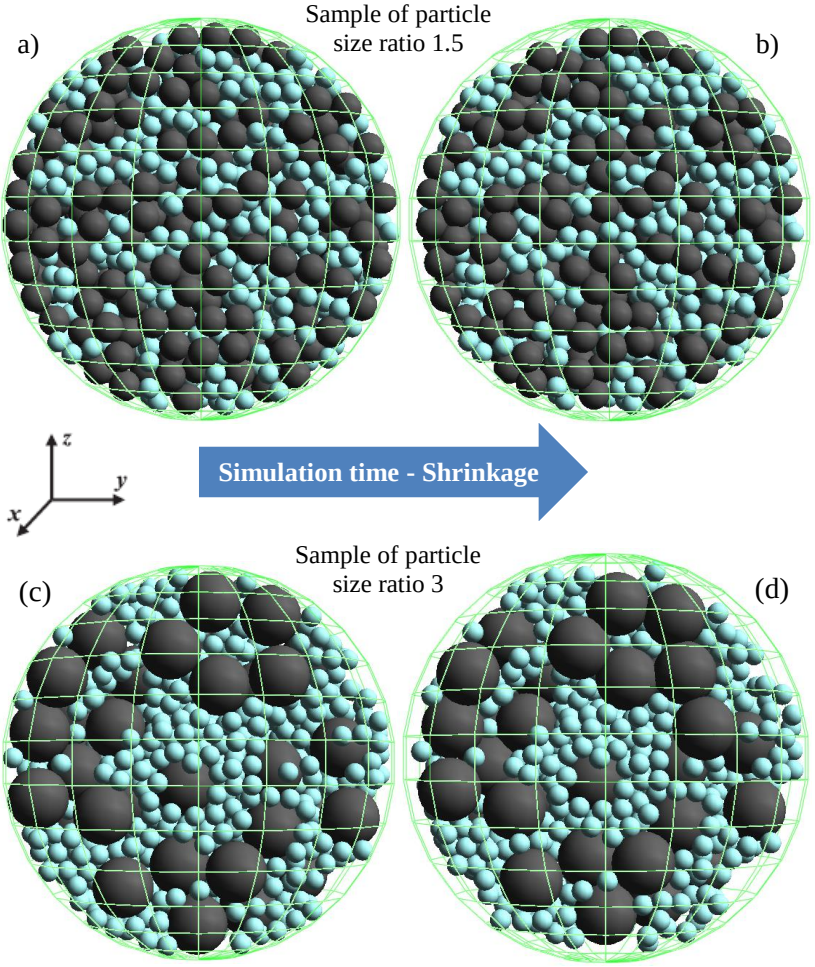

When the ratio 3.0 is analyzed in Figure 5.18 (c), the variation in the spatial distribution of volume is even more pronounced. The alumina particles are clearly clustered since the same nickel volume is distributed through larger particles. Moreover, a higher number of alumina is observed surrounding larger nickel particles, as exposed in the coordination number of Ni→Al_2O_3 contacts (see Figure 5.16). The

sample after the simulation (d) shows a noticeable distance of edges from the simulation box size. It means that the sample is shrinking during the simulation.

Comparing the samples 1.5 and 3.0 (Figure 5.18) to the sample 1.0 (Figure 5.7 (c) and (d) in Section 5.1.3), some substantial differences can be observed. The sintering behavior changes even though the nickel content is identical. While nickel and alumina particles sinter independently from each other in the sample 1.0, the densification can be noticed in a global manner in the samples 1.5 and 3.0. Those big empty defects (cracks) formed in the sample 1.0 throughout the simulation are not present in the final samples 1.5 and 3.0. As discussed in Section 5.2.1, smaller nickel particles have higher forces attracting each other. Thereby, larger nickel particles do not develop such high forces to cluster themselves and then alumina particles can keep attached by means of the viscous forces. Therefore, larger nickel particles densify more slowly but at the same time are able to "carry" alumina together and promote the densification globally.

These conclusions are supported by the quantitative analyses in the following section.

5.2.4 Global Densification

Figure 5.19 shows global relative density (RD) evolution of the bimodal samples with particle size ratio of 1.0, 1.5, 2.0, 2.5 and 3.0 over the simulation time.

As expected, RD increases for all samples along the process. In the beginning of the simulation a great portion of the densification occurs due to the rearrangements and low viscous forces between pairs of particles. This behavior is in accordance with the sintering theory (see Section 2.3.3). The densification curves in Figure 5.19 are similar to those in Figure 2.6.

Furthermore, it is possible to notice a tendency in Figure 5.19. The increase of the relative density is higher as the particle size increases. Indeed, this tendency can be in the other way around than one might expect. As it was stated and demonstrated previously, smaller particles have higher sintering activity to promote densification (see Section 5.2.1 about contact radius evolution). Then, larger particles should decrease the densification rate.

Figure 5.19: Global relative density evolution of all bimodal samples over time. The samples are referred to by the nickel-alumina particle size ratio.

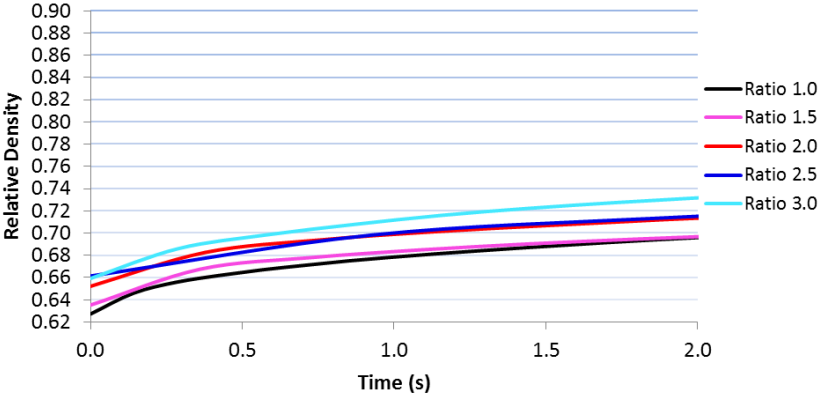

However, the behavior found in the densification results can be explained by the microstructural nature of interpenetrating structures and by the large difference between the kinetic parameters of metals and ceramics. This is discussed in detail in the next section.

5.2.5 Discussion of Bimodal Packings

The investigation of bimodal packing of composites has led to two different conclusions, which are not theoretically expected.

The first discussion regards the microanalysis of the samples with average contact radius and coordination number results. It has been found that larger particles have taken longer to attain the final ACR (65% of the particle radius), as observed in Figure 5.10. This is in agreement with the sintering theory, in which larger particles have lower surface energy and, thereby, less sintering activity. Therefore, the simulations of larger particles have demonstrated that sintering of pair of contacts is following the expected behavior.

On the other hand, the global densification results (Figure 5.19) do not show the same tendency described before. The samples with larger particles have reached higher relative density at the final of simulation. To explain such behavior, it is needed to recall two important facts. Firstly, the nickel volume fraction chosen to simulate to bimodal packings is 60% and, thereby, they are interpenetrating structures. Still, it is pointed out that for the monosized sample with 60 vol.% the metal and ceramic phase sintered independently from each

other and, as a consequence, it has shown the slowest densification among the samples (see section 5.1.3, 5.1.4 and 5.1.5). Many defects have been developed through the sample because the metal phase sintered too fast compared to the ceramic phase and they formed clusters of nickel particles. In other words, the monosized packing with 60% volume of nickel barely densified globally due to the great difference between the sintering kinetics of the materials.

In parallel, the simulations with bimodal have not shown development of such defects (cracks). As explained in Section 5.3.1, the sintering force attracting larger nickel particles is weaker and it is not enough to cluster them, as observed in the monosized sample. Moreover, the viscous forces (see Section 2.5), which act always against the movement, have an absolute value more significant for these lower sintering forces. Therefore, the alumina particles in the bimodal packing can keep attached to nickel ones and nickel particles are able to drive the densification of the whole sample.

Thus, composite materials characterized as interpenetrating structures and composed by two phases (metal and ceramic) with large differences in sintering potential, larger metal particles can drive more homogenous densification and fewer defects can be developed through the samples. Consequently, higher relative densities can be reached if compared to smaller metal particles due to the difference in the forces distribution.

6 CONCLUSIONS AND OUTLOOK

The software MUSEN has been used to simulate the sintering process after implementing a suitable contact model. It is possible to have access to the particles position, velocity, force, coordination number, as well as to see the shrinkage of the sample on the software 3D interface. Using the position over simulation time, it was possible to calculate the evolution of average contact radius between particles. Additionally one can observe particle rearrangement, crack development and calculate the relative density inside a specified volume of the sample. From the relative density calculation, it is possible to plot the densification curve of the process.

The special modeling approach proposed in this work has shown to be capable to simulate sintering of composites even in case of interpenetrating structures. The simulation results of the monosized packing can be divided in three different sintering behaviors: metal-controlled, ceramic-controlled and contact retarded sintering.

The metal-controlled samples have shown the highest densification rates and relative density evolution, as one might expect. The nickel particles have higher potential to sinter faster than alumina due to their kinetic parameters and surface energy. Hence, metal particles induce high forces to shrink the system and indirectly transfer forces to the sintering of ceramic phase. Therefore, the sintering of ceramic particles is supported by the metal phase. These interactions between metal and ceramic phase are important in densification of composites when materials with large differences of sintering kinetic are used.

Moreover, the addition of a second phase with low sintering activity (in this case alumina) reduces the overall densification in comparison to the pure metal and it takes longer to reach the same relative density. This result is in line with those found in the literature and confirms the correctness of the proposed approach.

The contact retarded sintering has been found for the samples characterized as interpenetrating structures. They have shown the lowest overall densification due to independent densification of metal and ceramic phase. It has led to large cracks through the samples and the initial structure has been lost. For this reason, it is recommended to use materials with similar diffusion parameters to achieve homogenous densification of an interpenetrating metal-ceramic composite. This investigation might be a topic for further works.

The simulation of bimodal packing with larger nickel particles and metal volume fraction of 60% has shown results that are more debatable. Individual analysis of particles, through the contact radius evolution, has shown slower growing for larger nickel particles, as expected. However, the global densification is higher for larger particles. This might be explained by the particle configuration in interpenetrating structures, in which metal and alumina form continuous network of particle and the distribution of forces throughout the system. Since smaller particles have higher forces attracting each other, the metal phase sinters quickly and forms long agglomerates of particles and the global densification barely take place. When larger nickel particles are present, the forces promoted by them are weaker. Thereby, the viscous force between nickel-alumina contacts is enough to keep these contacts attached and, finally, a global densification is observed.

Therefore, composite materials characterized as interpenetrating structures and composed by two phases (metal and ceramic) with large differences in sintering potential, larger metal particles can drive more homogenous densification and fewer defects can be developed through the samples. Consequently, higher relative densities can be reached if compared to smaller metal particles due to the difference in the forces distribution.

To confirm the correctness of the present modeling approach for bimodal packing, it is suggested for further works to carry out simulation of metal-matrix composites, instead of interpenetrating structures, with varying of the size of metal particles. Other suggestion for future work is to use samples with a distribution of particle size, which would make the simulation closer to reality. Still, it would be interesting to use nickel and zirconia as materials of the composite for further works. These materials have more similar sintering parameters and it would lead to more homogenous densification.

REFERENCES

[1] Chawla, K. K. (2012): Composite Materials. Science and Engineering. 3rd ed., Springer-Verlag New York, USA.

[2] German, R. M. (2014): Sintering: From Empirical Observations to Scientific Principles. 1st ed., Elsevier Butterworth-Heinemann, USA.

[3] Henrich, B.; Wonisch, A.; Kraft, T.; Moseler, M.; Riedel, H. (2007): Simulations of the influence of rearrangement during sintering. In *Acta Materialia* 55, pp. 753–762.

[4] Martin, C. L.; Schneider, L.C.R.; Olmos, L.; Bouvard, D. (2006): Discrete element modeling of metallic powder sintering. In *Scripta Materialia* 55, pp. 425–428.

[5] Olmos, L.; Martin, C. L.; Bouvard, D. (2009): Sintering of mixtures of powders, Experiments and modeling. In *Powder Technology* 190, pp. 134–140.

[6] Yan, Z.; Martin, C. L.; Guillon, O.; Bouvard, D. (2013): Effect of size and homogeneity of rigid inclusions on the sintering of composites. In *Scripta Materialia* 69, pp. 327–330.

[7] Black, J. T.; Kohser, R. A. (2008): Materials and Processes in Manufacturing. 10th ed., John Wiley & Sons, Inc. USA.

[8] Kang, S-J. L. (2005): Sintering. Densification, Grain Growth and Microstructure. 1st ed., Elsevier Butterworth-Heinemann, UK.

[9] Richerson, D. W. (2005): Modern Ceramic Engineering. Properties, Processing, and Use in Design. 3rd ed., CRC Press, USA.

[10] Fang, Z. Z. (2010): Sintering of advanced materials. Fundamentals and processes. 1st ed., Woodhead Publishing, UK.

[11] Kingery, W. D. (1992): Sintering from prehistoric times to the present. In *Solid State Phenomena* 25 & 26, pp. 1–10.

[12] Li, L.; Fang, Y.; Xiao, Q.; Wu, Y. J.; Wang, N.; Chen, X. M. (2014): Microwave Dielectric Properties of Fused Silica Prepared by Different Approaches. In *Int. J. Appl. Ceram. Technol.* 11, pp. 193–199.

[13] Cundall P.A.; Strack, O.D.L. (1979): A discrete numerical model for granular assemblies. In *Géotechnique* 29, pp. 47–65.

[14] Thornton, C.; Antony, S. J. (1998): Quasi-static deformation of particulate media. In *Phil. Trans. R. Soc. Lond. A* 356, pp. 2763–2782.

[15] Zhu, H. P.; Zhou, Z. Y.; Yang, R. Y.; Yu, A. B. (2008): Discrete particle simulation of particulate systems: A review of major applications and findings. In *Chemical Engineering Science* 63, pp. 5728–5770.

[16] Nosewicz, S.; Rojek, J.; Pietrzak, K.; Chmielewski, M. (2013): Viscoelastic discrete element model of powder sintering. In *Powder Technology* 246, pp. 157–168.

[17] Deen, N. G.; Van Sint Annaland, M.; Van der Hoef, M.A.; Kuipers, J.A.M. (2007): Review of discrete particle modeling of fluidized beds. In *Chemical Engineering Science* 62, pp. 28–44.

[18] An, X. Z.; Yang, R. Y.; Dong, K. J.; Zou, R. P.; Yu A.B. (2005): Micromechanical Simulation and Analysis of One-Dimensional Vibratory Sphere Packing. In *Physical Review Letters* 95 (20).

[19] Mishra, B. K.; Murty, C.V.R. (2001): On the determination of contact parameters for realistic DEM simulation of ball mills. In *Powder Technology* 115, pp. 290–297.

[20] Martin, C. L.; Montes, H. C.; Olmos, L.; Bouvard, D.; Bordia, R. K. (2009): Evolution of Defects During Sintering: Discrete Element Simulations. In *J. Am. Ceram. Soc.* 92, pp. 1435–1441.

[21] Wonisch, A.; Guillon, O.; Kraft, T.; Moseler, M.; Riedel, H.; Rödel, J. (2007): Stress-induced anisotropy of sintering alumina: Discrete element modeling and experiments. In *Acta Materialia* 55, pp. 5187–5199.

[22] Wonisch, A.; Kraft, T.; Moseler, M.; Riedel, H. (2009): Effect of Different Particle Size Distributions on Solid-State Sintering: A Microscopic Simulation Approach. In *J. Am. Ceram. Soc.* 92, pp. 1428–1434.

[23] Martin, C. L.; Bordia, R. K. (2009): The effect of a substrate on the sintering of constrained films. In *Acta Materialia* 57, pp. 549–558.

[24] Rasp, T.; Kraft, T.; Riedel, H. (2013): Discrete element study on the influence of initial coordination numbers on sintering behavior. In *Scripta Materialia* 69, pp. 805–808.

[25] Jagota, A.; Scherer, G. W. (1993): Viscosities and Sintering Rates of a Two-Dimensional Granular Composite. In *J. Am. Ceram. Soc.* 76, pp. 3123–3135.

[26] Jagota, A.; Scherer, G. W. (1995): Viscosities and sintering rates of composite packings of spheres. In *J. Am. Ceram. Soc.* 78, pp. 521–528.

[27] Verlet, L. (1967): Computer "experiments" on classical fluids. I. Thermodynamical properties of Lennard-Jones Molecules. In *Physical Review* 159, pp. 98-103.

[28] Chialvo, A. A.; Debenedetti, P. G. (1990): On the use of the Verlet neighbor list in molecular dynamics. In *Computer Physics Communications* 60, pp. 215-224.

[29] Skeel, R. D. (1993): Variable step size destabilizes the Stömer/Leapfrog/Verlet Method. In *Bit Num. Math.* 33, pp. 172-175.

[30] Zhu, H. P.; Zhou, Z. Y.; Yang, R. Y.; Yu, A. B. (2007): Discrete particle simulation of particulate systems: Theoretical developments. In *Chemical Engineering Science* 62, pp. 3378–3396.

[31] Bouvard, D.; McMeeking, R. M. (1996): Deformation of interparticle necks by diffusion-controlled creep. In *J. Am. Ceram. Soc.* 79, pp. 666–672.

[32] Riedel, H.; Zipse, H.; Svoboda, J. (1994): Equilibrium pore surfaces, sintering stresses and constitutive equations for the intermediate and late stages of sintering - II Diffusional densification and creep. In *Acta Metall. et Mater.* 42, pp. 445–452.

[33] Raj, R.; Ashby, M. F. (1975): Grain Boundary Sliding and Diffusional Creep. In *J. Materials Science* 10, pp. 1889–1903.

[34] Coble, R. L. (1958): Initial Sintering of Alumina and Hematite. In *J. Am. Ceram. Soc.* 41, pp. 55–62.

[35] Pan, J.; Le, H.; Kucherenko, S.; Yeomans, J. A. (1998): A Model for the Sintering of Spherical Particles of Different Sizes by Solid State Diffusion. In *Acta Materialia* 46, pp. 4671–4690.

[36] Parhami, F.; McMeeking, R. M.; Cocks, A. C. F.; Suo, Z. (1999): A Model for the Sintering and Coarsening of Rows of Spherical Particles. In *Mechanics of Materials* 31, pp. 43–61.

[37] Dosta, M.; Antonyuk, S.; Heinrich, S. (2013): Multiscale simulation of agglomerate breakage in fluidized beds. In *Ind. Eng. Chem. Res.* 52, pp. 11275-11281.

[38] Dosta, M.; Heinrich, S.; Werther, J. (2010): Fluidized bed spray granulation: Analysis of the system behavior by means of dynamic flowsheet simulation. In *Powder Technology,* 204, pp. 71-82.

[39] Martin, C. L.; Bouvard, D.; Schima, S. (2003): Study of particle rearrangement during powder compaction by the Discrete Element Method. In *J. Mech. Phys. Solids* 51, pp. 667–693.

[40] Lu, K. (2008): Sintering of nanoceramics. In *International Materials Reviews* 53, pp. 21–38.

[41] Gómez, S. Y.; da Silva, A. L.; Gouvêa, D.; Castro, R. H. R.; Hotza, D. (2016): Nanocrystalline yttria-doped zirconia sintered by fast firing. In *Materials Letters* 166, pp. 196-200.

[42] Hotza, D.; García, D. E.; Castro, R. H. R. (2015): Obtaining highly dense YSZ nanoceramics by pressureless, unassisted sintering. In *International Materials Reviews* 60, pp. 353–375.

[43] Possamai, T. S.; Oba, R.; Nicolau, V. P.; Hotza, D.; Garcia, D. E. (2012): Numerical simulation of the fast firing of alumina in a box furnace. In *Journal of the American Ceramic Society* 95, pp. 3750–3757.

[44] Nakada, Y.; Kimura, T. (1997): Effects of shape and size of inclusions on the sintering of ZnO-ZrO_2 composites. In *J. Am. Ceram. Soc.* 2, pp. 401–406.

[45] Pasquarelli, R. M.; do Rosário, J. J.; Rath, L.; Schneider, G. A.; Janssen, R. (2015): High temperature behavior of monodisperse porosity in alumina films. In *J. Eur. Ceram. Soc.* 14, pp. 3917–3926.